

**Tailored Flower-Like Ni-Fe-MOF-Derived Oxide
Composites: Highly Active and Durable
Electrocatalysts for Overall Water Splitting**



Zoya Iqbal

Reg no: 365037

This thesis work is submitted as a partial fulfillment of the requirements

for the degree of

MS Physics

Supervised By

Dr Fahad Azad

Department of Physics

School of Natural Sciences (SNS)

National University of Sciences and Technology (NUST), H-12

Islamabad, Pakistan

Year 2024

TK
MISCELLANEOUS

THESIS ACCEPTANCE CERTIFICATE

Certified that final copy of MS thesis written by Zoya Iqbal (Registration No. 00000365037), of School of Natural Sciences has been vetted by undersigned, found complete in all respects as per NUST statutes/regulations, is free of plagiarism, errors, and mistakes and is accepted as partial fulfillment for award of MS/M.Phil degree. It is further certified that necessary amendments as pointed out by GEC members and external examiner of the scholar have also been incorporated in the said thesis.

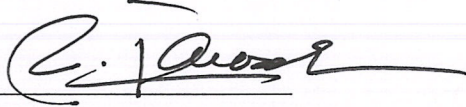
Signature:  _____

Name of Supervisor: Dr. Fahad Azad

Date: _____

Signature (HoD):  _____

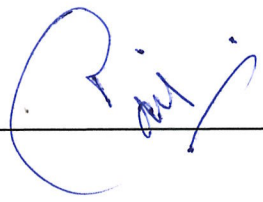
Date: 8/8/2024

Signature (Dean/Principal):  _____

Date: 09.08.2024

National University of Sciences & Technology**MS THESIS WORK**

We hereby recommend that the dissertation prepared under our supervision by: Zoya Iqbal, Regn No. 00000365037 Titled: Tailored Flower Like Ni-Fe-MOF-Derived Oxide Composites : Highly Active and Durable Electrocatalyst for Overall Water Splitting be Accepted in partial fulfillment of the requirements for the award of **MS** degree.

Examination Committee Members1. Name: PROF. MANZAR SOHAILSignature: 2. Name: DR. MUHAMMAD ADIL MANSOORSignature: Supervisor's Name DR. FAHAD AZADSignature: 

Head of Department

8/8/2024

Date

COUNTERSIGNEDDate: 09.08.2024

Dean/Principal

DEDICATION

In the name of Allah, the Most Gracious, the Most Merciful,

I humbly dedicate this thesis to the beloved Prophet Muhammad (peace be upon him).

His timeless wisdom, boundless compassion, and unwavering dedication to the service of humanity inspire every aspect of my life. It is through his noble example that I have learned the true essence of living for others. May this work on hydrogen production, aimed at advancing the well-being of mankind, reflect the light of his teachings and contribute to a brighter, more sustainable future for all.

To my beloved Parents and my brothers who have been always my source of strength.

To my supervisor who always shared her words of guidance, advice, and encouragement.

ACKNOWLEDGEMENTS

الْحَمْدُ لِلَّهِ

All praises and thanks be to **Allah Almighty my Rabb** for blessing me with intellect, courage, and stamina to complete my research work. Nothing would have been possible without His mercy and grace.

I pay my deepest gratitude to my supervisor **Dr. Fahad Azad** for his guidance, valuable cooperation for my research work and moral support throughout the research journey. He played a pivotal role in accomplishment of this project.

He always managed to guide me in the right research direction. I am very thankful to him.

I pay my cordial thanks to my GEC members **Dr. Manzar Sohail & Dr. Adil Mansoor** for their assistance, knowledge sharing and guidance. I am thankful to HOD Dr. Rizwan Hussain for ensuring the availability of a positive research environment.

I would also like to acknowledge all the faculty and lab staff of SNS for being cooperative and kind.

I am thankful to the School of Chemical and Materials Engineering (SCME) for facilitating me in characterization of materials.

I am grateful to Allah for blessing me with a family who has backed me and has given me courage, love, and support that I needed. I am thankful to **my parents, brothers** and all my family members and friends y for always pushing me ahead.

Zoya Iqbal

Abstract

To achieve a carbon-neutral future, it is essential to develop sustainable methods for hydrogen production by water electrolysis. Efficient and eco-friendly hydrogen production through electrolysis demands significant energy input. This high energy requirement necessitates the use of catalysts to reduce energy consumption making electrolysis process to be economically viable. In this pursuit, we synthesized a bifunctional electrocatalyst ($\text{Fe}_3\text{O}_4/\text{NiO-C}$) with improved catalytic performance using Ni-Fe-MOF as the precursor material. The $\text{Fe}_3\text{O}_4/\text{NiO-C}$ catalyst demonstrated a substantial enhancement in electrochemical performance, faster reaction kinetics, and long-term durability compared to pristine Ni-Fe-MOF. It achieved an exceptionally high current density of 500 mA cm^{-2} at an overpotential of 280 mV for the oxygen evolution reaction (OER) and 50 mA cm^{-2} at 182.5 mV for the hydrogen evolution reaction (HER), with Tafel slopes of 59.0 mV/dec and 53 mV/dec, respectively. Additionally, it showed extended electrochemical stability, maintaining 86% performance for OER and 93% for HER after 24 hours of chronoamperometry test. The outstanding performance of $\text{Fe}_3\text{O}_4/\text{NiO-C}$ is due to its unique composition, interfacial interactions, and its high surface area and porosity. This research emphasizes the significance of MOF-derived transition metal oxides as highly efficient, active, and stable bifunctional electrocatalysts for water-splitting.

Keywords: MOF-derived Oxides, Fe_3O_4 , NiO, HER, OER, Electrocatalyst

Table of Content

DEDICATION.....	2
ACKNOWLEDGEMENTS.....	3
Abstract.....	4
Keywords: MOF-derived Oxides, Fe ₃ O ₄ , NiO, HER, OER, Electrocatalyst	4
Chapter 1.....	10
Introduction	10
The research objective is as follows:.....	21
Chapter 2.....	23
Literature Review	23
Table 1: Comparison of HER and OER activity for Ni-Fe-MOF, Fe ₃ O ₄ /NiO/Ni-Fe-MOF and Fe ₃ O ₄ /NiO-C electrocatalyst with other recently reported Fe and Ni based electrocatalysts.	34
Chapter 3.....	36
Apparatus and Characterization Techniques	36
Apparatus Required	36
Digital weight balance	36
Hotplate	37
Autoclave.....	37
Characteristics of an ideal hydrothermal autoclave.....	38
Electric Oven	38
Centrifuge machine.....	39

Characterization Techniques	40
X-ray Diffraction (XRD)	40
Fourier Transform Infrared Spectroscopy (FT-IR)	41
Scanning Electron Microscopy (SEM).....	42
Energy Dispersive X-Ray Spectroscopy (EDX)	43
Chapter 4.....	45
Materials and Methods	45
Materials	45
Synthesis.....	45
a. Synthesis of Ni-Fe MOF.....	45
b. Synthesis of Fe ₃ O ₄ /NiO-C	46
Procedure:.....	46
Preparation of Nickel Foam Substrate:.....	46
Chapter 5.....	45
5.1. Characterization.....	48
5.1.2. Thermogravimetric Analysis (TGA)	50
5.1.3. Fourier-transform infrared FTIR	51
5.1.4. Vibrating Sample Magnetometer (VSM)	52
5.2. Electrochemical Analysis	59
Conclusion	66
Chapter 6.....	66
Future Recommendation.....	66
Published Articles.....	66
Articles in Writing Process.....	66
References	66

Table of Figures

Figure 1: Hydrogen generation sources throughout the globe (natural gas 48%, oil 30%, coal 18% and Electrolysis 4%). ⁹⁷	Error! Bookmark not defined.
Figure 2: Daniel cell, an electrolytic cell consisting of two half reactions, two electrodes, a salt bridge and a voltage source	14
Figure 3: Chlor-Alkali Membrane Electrolyzer Cell to a Wind Energy Source. ⁹⁹	16
Figure 4:proton exchange membrane fuel cell schematic diagram ³⁷	17
Figure 5: Diagram of SOEC cell	18
Figure 6:Photoelectrochemical water splitting(a) Equation of PEC reaction (b)Mechanism of PEC water splitting	20
Figure 7:Mechanism of electrochemical water splitting	21
<i>Figure 8. Hot plate with a beaker containing blue solution.</i>	37
Figure 9: Stainless steel autoclave with Teflon beaker generally used for solvothermal or hydrothermal synthesis	38
Figure 10: Electric oven with temperature ranges up to 400°C.....	39
Figure 11: Centrifuge machine used for washing process after hydrothermal synthesis.	39
<i>Figure 12. Image of XRD machine</i>	41

Figure 13: Working of FTIR spectrometer. ⁹⁸	42
Figure 14: Schematic of working of Scanning electron microscope. ⁷⁸	43
Figure 15: Schematic explaining EDX phenomenon ¹⁰⁰	44
Figure 16: Synthesis Mechanism of Ni-Fe-MOF, Fe ₃ O ₄ /NiO/Ni-Fe-MOF and Fe ₃ O ₄ /NiO-C	45
Figure 17: XRD pattern of pure Ni-Fe-MOF, Fe ₃ O ₄ /NiO/Ni-Fe-MOF and Fe ₃ O ₄ /NiO-C	49
Figure 18: XRD pattern of Fe ₃ O ₄ /NiO-C after 24 hours chronoamperometry test (a)OER and (b)HER	50
Figure 19: Thermogravimetric analysis of Ni-Fe-MOF, Fe ₃ O ₄ /NiO/Ni-Fe-MOF and Fe ₃ O ₄ /NiO-C	50
Figure 20 : FTIR spectra of all the synthesized sample Ni-Fe-MOF, Fe ₃ O ₄ /NiO/Ni-Fe-MOF and Fe ₃ O ₄ /NiO-C.....	51
Figure 21: VSM graph of Ni-Fe-MOF, Fe ₃ O ₄ /NiO/Ni-Fe-MOF and Fe ₃ O ₄ /NiO-C	52
Figure 22: (a-d) Specific surface area and porosity of Ni-Fe-MOF, Fe ₃ O ₄ /NiO/Ni-Fe-MOF and Fe ₃ O ₄ /NiO-C was studied through BET analysis	53
Figure 23:(a-f) SEM images of Ni-Fe MOF, Fe ₃ O ₄ /NiO/Ni-Fe-MOF and Fe ₃ O ₄ /NiO-C and (g-h) TEM images further confirm the interlinked spherical particles of iron and nickel oxide in Fe ₃ O ₄ /NiO-C, along with (i) SAED patterns confirming the presence of Fe ₃ O ₄ and NiO in the nanocomposite.....	56

Figure 24:(a-c) EDX with color mapping confirming the presence of elements (C, O, Fe and Ni) in all the three samples (Ni-Fe-MOF, Fe₃O₄/NiO /Ni-Fe-MOF and Fe₃O₄/NiO -C).57

Figure 25: SEM images of Fe₃O₄/NiO-C (a) before chronoamperometry, (b) after OER chronoamperometry, (c) after HER chronoamperometry.57

Figure 26: EDX graphs and mapping of Fe₃O₄/NiO-C after OER and OER stability (a, c) after OER chronoamperometry (b, d) after HER chronoamperometry58

Figure 27: (a-d) Electrochemical measurements showing comprehensive analysis towards OER for Ni-Fe-MOF, Fe₃O₄/NiO/Ni-Fe-MOF and Fe₃O₄/NiO-C. (a) over potential, (b) Tafel slope, (c) comparison of overpotential at different current densities of all the samples, (d) chronoamperometry Fig. (a-e) unveils the potential of Fe₃O₄/NiO-C for OER as an electrocatalyst keeping in view its overpotential, Tafel slope, stability and conductivity. Fig. (f) shows the OER overpotential comparison of MOF-derived Fe₃O₄/NiO nanocomposites with other iron and nickel oxide-based electrocatalysts.^{69,71,72,74-76}61

Figure 28:(a-f) Electrochemical measurement of Ni-Fe-MOF, Fe₃O₄/NiO/Ni-Fe-MOF and Fe₃O₄/NiO-C as HER catalyst. The potential of Fe₃O₄/NiO-C compared to pristine Ni-Fe-MOF for HER is demonstrated by its lowest overpotential (a-c), Tafel slope (b), high stability (d,f) and faster reaction kinetics indicated by smallest semicircle in EIS conducted at -0.15 V (e).....63

Figure 29:Cyclic voltammetry curves showcasing the redox peaks of Ni-Fe-MOF, Fe₃O₄/NiO/Ni-Fe-MOF and Fe₃O₄/NiO-C electrocatalyst.....64

Chapter 1

Introduction

1. Introduction

As the reserved fossil fuels are declining rapidly, the energy supplied rate of fossil fuel is also diminishing, but the demands of the fundamental energy are continuously increasing more and more with the day by day rise in world's population, which will be leaping up by a factor of 26% that is approximately 9.7 billion by 2050.^{1,2} There is also a serious concern that fossil fuels are not environment-friendly and may be highly damaging to humans, plants and other creations as they can expedite greenhouse effect, cause air pollution, water pollution, as well as leading to severe climate change. One of the root causes of the global warming is greenhouse gases, according to an estimate if global warming pursues to increase at the ongoing rate, then between 2030-2052, global temperature is probably increased by 1.5 °C ensue almost 3.8 m rise in the sea level.³ To address these concerns, significant steps must be taken to explore clean, renewable substitutions as a reliable source of energy so, the conversion of economical fossil fuel systems to economical renewable energy systems requires the establishment of highly efficient, cost-effective and environmentally friendly catalysts as a renewable energy source.⁴⁻⁶

1.1. Energy Crisis

Energy resources play a vital role in economic security of any developing country. The countries with progressive economies are now considering a new concept of “natural security”. This concept defines the availability of natural resources. The availability is affordable. These natural resources must be environmentally friendly, reliable, and available in sufficient amounts. They are important for the economy of a country as the economy of a country is measured directly by the energy production of that country.⁷ The progress and prosperity of a country is directly indicated by the energy requirements. Energy consumption is the main source to run any country. It is also the biggest need of human being now a days. It is being used for industrial as well as domestic purposes. It is being used for cooking purposes. It is also used for pumping water. Recent studies show that there is a rise of 1.56% in economic growth for 10% increase in energy consumption⁷. The sources of energy can be divided into two categories. These are renewable and non-renewable energy resources. The non-renewable

energy resources are those energy resources that can be reproduced. They include natural gas, coal and crude oil ⁸. While the renewable energy sources are those that can be reproduced. They include wind power, solar power, hydrogen, and biomass. There is a huge rise in the demand for energy due to the industrial evolution and for domestic purposes. It is because of the high population growth throughout the world. There is a lot of increase in human standard. Economic security of a country depends upon its energy resources especially in case of developing countries. It is the reason that we are using more energy as fuel for vehicles. A survey was done in 2013 ⁸. This survey shows that 82.5% of the energy is being obtained from fossil fuels. Therefore, fossil fuels are being depleted. Geologists suggest that if fossil fuels will be continued to be extracted at the same rate, there will be shortage of fuel and energy sources in near future and the results will be worst. There will be a crisis. The total energy supply to Pakistan was 64.5 million in 2013. The fraction shared by the gas is 48.2%, oil's share is 32.5%, coal 6%, and LPG 0.5% ⁹.

Pakistan imports crude oil. It costs us a lot as our economy is low. While the use of fossil fuels also effects environment. CO, CO₂, SO_x, and NO_x are polluting our environment. Similarly, these conventional sources of energy are being depleted day by day. But our industrial demand is high. So, it is creating a supply-demand gap. That is why we need alternative sources of energy.

Amongst various investigated solutions for clean energy resources, H₂ as a clean fuel is the most proficient and viable green source of energy as its gravimetric density is much higher than the gravimetric energy density of petroleum. Next to that hydrogen as a fuel is excellent because it has a high efficiency, gives nontoxic, exhaust product, renewable and we can use it for energy storage.^{10,11} Despite the fact that hydrogen (H₂) is expected to be the most sustainable energy solution, hydrogen production processes are still in the development phase for commercial use. Today, fossil fuels constitute the main source of hydrogen produced on an industrial and commercial scale. Most of the commercial production of hydrogen now occurs in petroleum refineries or in the chemical industry. Hydrogen is primarily used as a raw material in petroleum refineries and other applications, including plastics and resins.¹² About 96 percent of the global hydrogen supply comes from the vapor reforming of oil and natural gas, as well as coal gasification.^{13,14} In order to abolish dependence on fossil fuels, hydrogen production would have to come from bountiful and clean sources, with environmentally friendly processes.

Water splitting is an important approach to renewable substitute for hydrogen production.¹⁵ About 70 percent of the earth surface is covered with water so it can be the amplest source of

Hydrogen production as it is of no harm to our environment and can be recycled back to H₂O. The other product of water splitting is O₂ that has only positive influence on the Atmosphere and its very useful for other applications which enhances the profit gain by electrolysis of H₂O. Currently only 4 percent of H₂ is produced by the electrolysis of H₂O. The reason for the low production rate of Hydrogen is that catalysis of water requires high energy to break the hydrogen bonding present between the H₂O molecules. Water splitting involves 2 types of reaction inside the cell in the presence of electrolyte on the bases of reduction and oxidation of H₂O on cathode and anode respectively. The reduction reaction is known as HER as hydrogen evolved in this half of the cell and the oxidation occurs on anode is known as OER as it evolves Oxygen.

The kinetics of OER and HER are very slow, so they always require a catalyst to break the strong bonds between H-O in H₂O. Usually, the catalyst is Nobel metals like Ruthenium, Platinum etc. But Nobel metals are highly expensive, hard to reserve, and poor sustainability, which restrains us from using them for electrolysis at commercial scale.^{16,17} Transition metals like Fe, Ni and Co which are plentiful, stable and have special catalytic activity can be a preferable choice in comparison with highly expensive Nobel metals.^{18,19} In addition to catalyst composition, chemical structure and morphology, both are substantial in determining the catalytic activities for efficient hydrogen production by water-splitting. Because of the ease of access to the pores, the short charge transfer distance, the exposed active sites, and the smooth diffusion of reactants and products from the catalytic sites, porous micro-nanostructures exhibit excellent photocatalytic performance.²⁰⁻²⁷

Metal-organic frameworks (MOFs), which combine metal centers with organic linkers to form a structure, are being heralded as an emerging class of materials. Due to their higher porosity (90% free volume), flexible structure, compositional tunability, exceptionally high surface area, and crystallinity, they have remarkable optoelectronic, electrical, and catalytic capabilities. Their value has lately been used in a wide range of applications, including water splitting, Carbon dioxide absorption, as sensors, and adsorption.²⁸⁻³³

Additionally, a thorough examination has been done on MOFs as a powerful catalyst for the electrochemical and photoelectrochemical evolution of hydrogen by water - splitting. Intrinsically MOF's ability to retain their functional groups and structures after modifications made to their structural elements using synthetic synthesis strategies transforms them into powerful catalysts for water-splitting.³⁴ MOFs can be designed for efficient and improved catalytic sites in hydrogen production, introducing light sensitizing functional groups, band gap

adjustment, and maintaining a photoelectric charge.

As frameworks for the synthesis of functionalized materials (such as porous carbon, M-sulphides, M-oxides, and C metal/M-oxide hybrids), MOFs have certain various benefits over typical semiconductor catalysts. Most of the time, the structure morphologies of the original MOFs are maintained in the derivatives, and increased catalytic performance is frequently seen.^[34] Additionally, MOFs and their derivatives can be used as support in the creation of well-planned nano-catalysts.^{35,36}

Numerous studies have been conducted in the last few years on the use of MOFs as photoelectrochemical and electrochemical photocatalyst for electrolysis of H₂O. This field of study will continue to draw more attention. This makes it highly important to examine the progress and difficulties faced by MOF-based composites as catalyst for water-splitting. The goal of this paper is to provide a thorough review of the investigation and development of MOF-derived catalysts for PEC and EC water splitting and their future advancements.

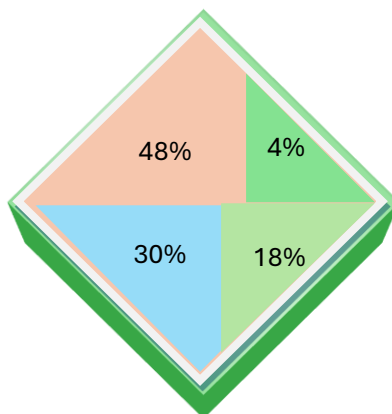


Figure 1: Hydrogen generation sources throughout the globe (natural gas 48%, oil 30%, coal 18% and Electrolysis 4%).⁹⁷

1.2. *Electrolysis of Water*

Electrolysis is the non-spontaneous chemical decomposition of water into its constituent components hydrogen and oxygen driven by the application of an external electric current. This process takes place in an electrolytic cell where water act as an electrolyte and electrode performs the redox reaction.



1.3. *Key components of water splitting*

Key components of water splitting are electrolytic cells, electrolyte with different pH values,

electrodes with different material type and catalyst for speed up the reaction process.

i. Electrolysis cell

Electrolysis cells play an important role in the production of hydrogen and oxygen for the development of clean and sustainable energy technologies. Ongoing research focuses on improving efficiency, reducing costs, and integrating electrolysis cells with renewable energy sources to enhance the environmental sustainability of hydrogen production. Electrolysis cells play a key role in various industrial processes, including metal extraction, electroplating, and the production of gases. There are different types of electrolytic cells based on their applications and configurations. Some common types are:

a) Aqueous Electrolysis Cells:

An aqueous electrolytic cell is a type of electrolytic cell in which the electrolyte is an aqueous (water-based) solution. Water serves as the medium in these cells, through which ions move, and the electrolyte many times contains dissolved salts or acids to enhance conductivity.

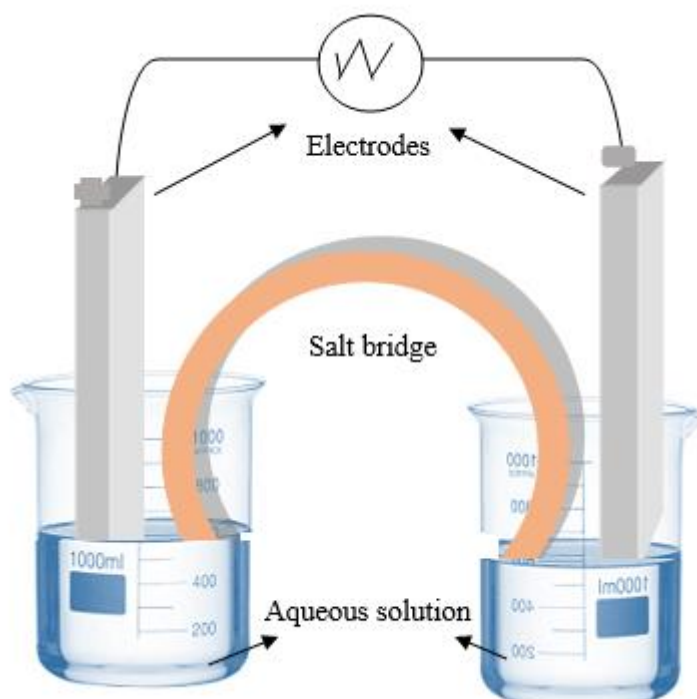


Figure 2: Daniel cell, an electrolytic cell consisting of two half reactions, two electrodes, a salt bridge and a voltage source. Aqueous electrolytic cells are commonly used for the electrolysis of water to produce hydrogen and oxygen and the deposition of metals through electroplating.

Electrodes reactions

Overall reaction: $2\text{H}_2\text{O} (\text{l}) \rightarrow 2\text{H}_2 (\text{g}) + \text{O}_2 (\text{g})$

Anode reaction: $2\text{H}_2\text{O} (\text{l}) \rightarrow \text{O}_2 (\text{g}) + 4\text{H}^+(\text{Aqua}) + 4\text{e}^-$

Cathode reaction: $2\text{H}_2\text{O} (\text{l}) + 4\text{e}^- \rightarrow 2\text{H}_2 (\text{g}) + \text{OH}^- (\text{Aqua})$

b) Industrial Electrolysis Cells:

Industrial electrolysis cells are used for large-scale industrial processes. For example, electrolysis of molten sodium chloride (Downs cell) to produce sodium and chlorine.

c) Electroplating Cells:

Electroplating is an adaptable widely used industrial process, inside electroplating cells, a metal object is coated with a thin layer of another expensive metal using electrolysis. The specific parameters can be adjusted based on the desired properties of the plated object. Electroplating helps to improve the aesthetics, durability, and functionality with a wide range of other applications e.g. enhancing appearance (decorative plating of jewelry, silverware, and ornaments), corrosion Protection (Plating metals like zinc onto iron or steel to provide a protective layer), electrical conductivity (coating connectors and electrical components with metals like gold or silver for improved conductivity) preventing tarnishing (Plating silver objects to prevent tarnishing), hardening surfaces (depositing hard metals like chromium onto objects to improve durability) and creating reflective surface (plating metals like aluminum onto glass to create mirrors).

d) Chlor-Alkali Electrolysis Cells:

Chlor-alkali electrolysis cells is used to produce chlorine, sodium hydroxide, and hydrogen. For example: electrolysis of sodium chloride (NaCl) solution in a mercury cell or membrane cell.

e) Fuel Cells:

Fuel cells are used for generating electrical energy from the reaction between a fuel and an

oxidant. Fuel cells, which only produce water as a byproduct and are an electrochemical device used to transform chemical energy into electricity, have drawn a lot of interest since they are ecologically benign. Direct Methanol Fuel Cells (DMFC) are noteworthy for being an outlier, since they produce CO₂ in addition to water as byproducts. Hydrogen fuel cells, where hydrogen reacts with oxygen to produce electricity, water, and heat. Fuel cells serve as chambers for continuing electrochemical processes, in contrast to traditional batteries, which are disposed of after chemical usage and become outdated.

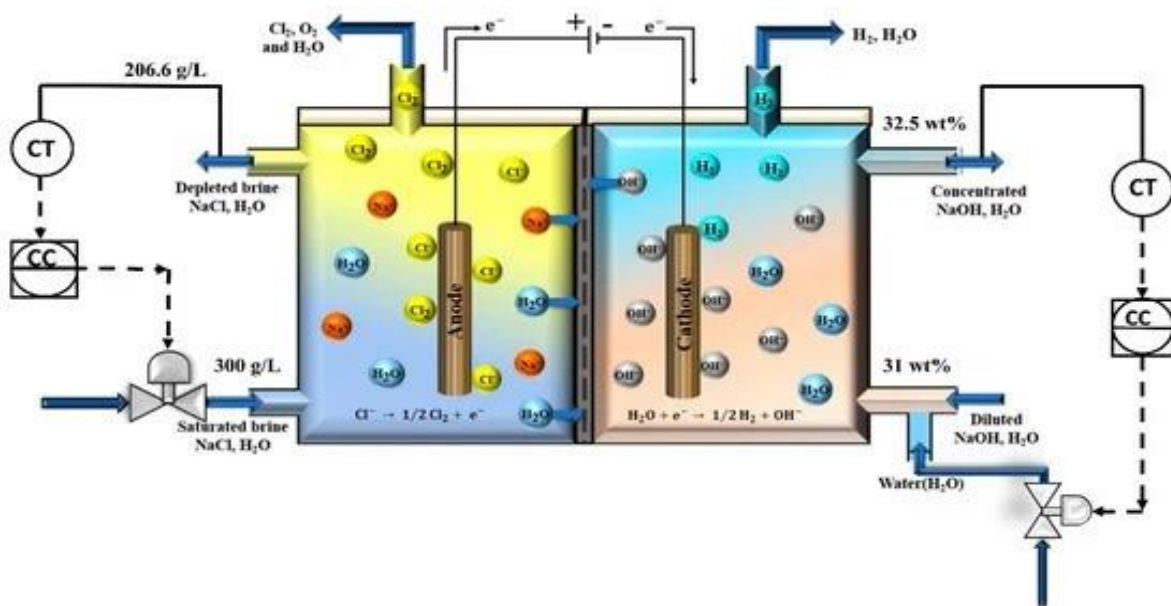


Figure 3: Chlor-Alkali Membrane Electrolyzer Cell to a Wind Energy Source.⁹⁹

f) Proton Exchange Membrane (PEM) Electrolysis Cells:

Proton exchange membrane (PEM) electrolysis cells used for the electrolysis of water to produce hydrogen and oxygen. It utilizes a solid polymer electrolyte membrane, operates at lower temperatures compared to traditional electrolysis cells.

g) Hall-Héroult Cell:

Hall-Héroult Cell is used for the industrial production of aluminum from aluminum oxide. It is also known as high-temperature molten salt electrolysis.

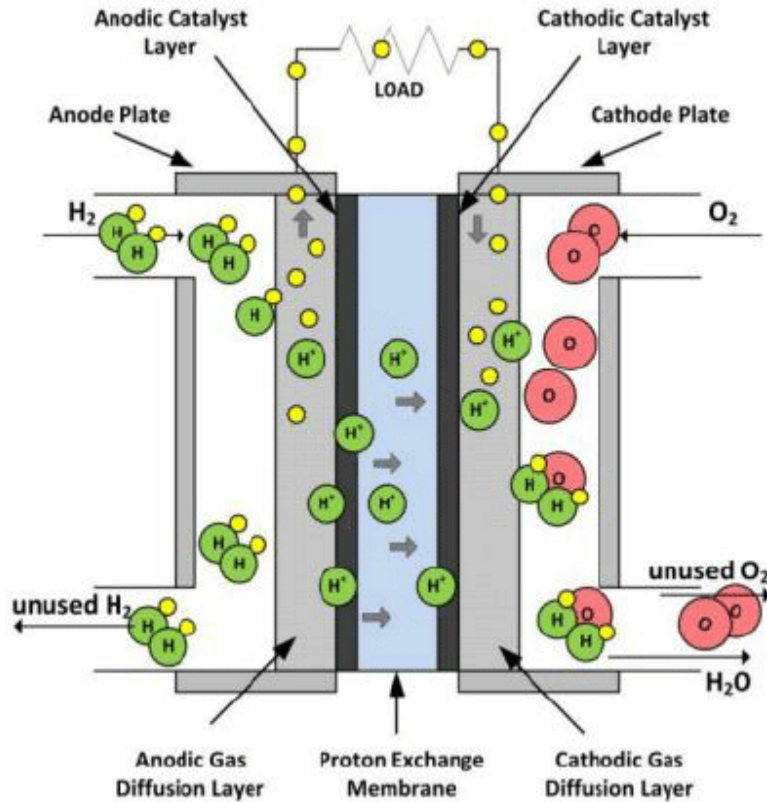


Figure 4:proton exchange membrane fuel cell schematic diagram³⁷

h) Mercury Cell:

Electrolysis of sodium chloride for chlorine and sodium hydroxide production is carried out in Mercury cell. It employs a mercury cathode to prevent the formation of sodium amalgam.

i) Downs Cell:

Sodium and chlorine are produced by the electrolysis of molten sodium chloride in downs cell. It is a high-temperature electrolysis using a carbon anode and iron cathode.

j) Solid Oxide Electrolysis Cell (SOEC):

SOEC is used for high-temperature electrolysis. SOEC operates at elevated temperatures, typically in the range of 600–1000°C, and is capable of producing hydrogen from steam.

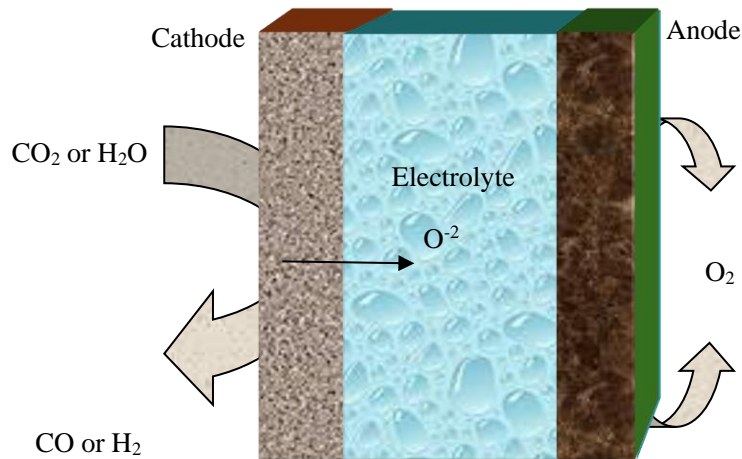


Figure 5: Diagram of SOEC cell

ii. *Electrolyte*

The electrolyte is the medium through which ions move between the electrodes. In the context of water electrolysis, the electrolyte is water itself, and sometimes additional ions are introduced to enhance conductivity by adding acid or bases in water to make it acidic or basic. Most common electrolyte solution is KOH in deionized water which is basic solution with pH 14.

iii. *Electrodes*

The cell contains two electrodes, one is anode and the other one is cathode, immersed in an electrolyte. Anode is the electrode where oxidation (loss of electrons) occurs while cathode is the electrode where reduction (gain of electrons) takes place.

iv. *Electrical Power Source:*

An external electrical power source, such as a battery or power supply, is connected to the electrodes. This source provides the energy needed to drive the electrolysis reactions.

v. *Role of catalyst in electrochemical water splitting*

Electrolysis occurs at the electrodes of an electrolytic cell, and catalysts play a crucial role in enhancing the efficiency of this process. In the context of water splitting, there are two half-

reactions: the oxygen evolution reaction (OER) occurring at the anode and the hydrogen evolution reaction (HER) occurring at the cathode. Catalysts are employed to facilitate these reactions and reduce the energy input required for the overall water splitting process.

In electrochemical water splitting catalysts lower the activation energy barriers and increases the reaction rate making OER easier to proceed and reducing the overpotential required to drive the reactions which results in more energy efficient process. Catalysts can also facilitate the transfer of electrons during electrochemical reactions. This is particularly important in the OER, where multiple electron transfer steps are involved. It modifies the surface properties of the electrodes, creating active sites for water adsorption and facilitating the dissociation of water molecules into hydrogen and oxygen.

This modification enhances the overall efficiency of the electrochemical cell. Some parameters are crucial in the selection of a catalyst. Catalysts need to be compatible with the electrode materials and electrolyte used in the system. Compatibility ensures good adhesion, durability, and performance of the catalyst in the electrolysis cell. Moreover, catalysts need to be stable under the harsh electrochemical conditions of water splitting, which often involve corrosive environments. A good catalyst should exhibit long-term stability to ensure sustained performance over extended periods of operation.

Common catalysts used in water splitting include metal oxides, metal chalcogenides, and other transition metal-based compounds. Additionally, research is ongoing to discover and develop new and more efficient catalyst materials for advancing the field of electrochemical water splitting.

1.4. Kinetics of Water splitting

Fujishima and Honda introduced the concept of PEC water-splitting in 1972.³⁸ Turner and Khaselev demonstrated solar to hydrogen transformation in PEC cells with an efficiency of 12.4% in 1998. This demonstrated clearly the power of PEC for hydrogen production using solar energy for water electrolysis.³⁹ When we put in an electrolytic cell with electrolyte solution, a PEC catalyst with the right characteristics can split water into its component hydrogen and oxygen by conversion of light energy from sunlight into electrochemical energy.

i. Basic Principle of PEC water splitting

An efficient photocatalyst is used in Hydrogen evolution, which operates on the idea of

capturing sunlight to break H₂O into O₂ and H₂. Semiconducting materials seem to be presently the focus of in-depth research on photocatalyst. When a photon strikes at the surface of a catalyst, electrons move from the VB to the CB band (reduction process), forming holes in the VB (oxidation reaction).⁴⁰

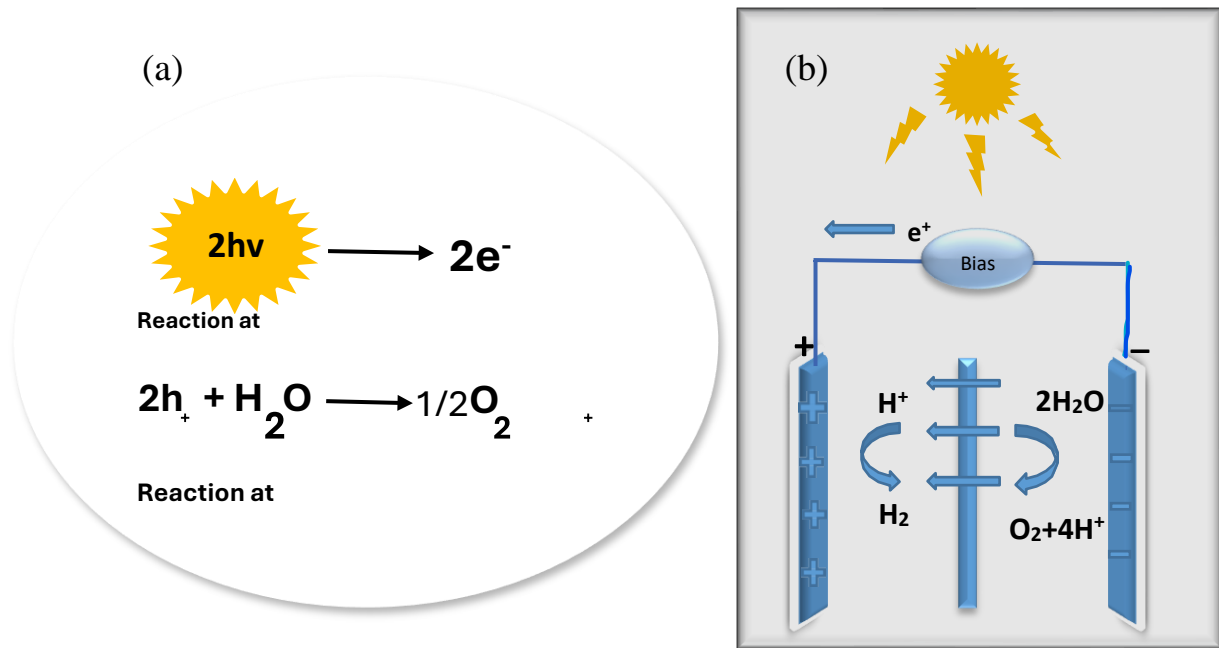


Figure 6:Photoelectrochemical water splitting(a) Equation of PEC reaction (b)Mechanism of PEC water splitting

These electron/hole pairs then function as charge carriers. Aqueous electrolyte, cathode and anode the two electrodes, and an external circuit make up the PEC cell's basic components. Electronic charge carriers, such as electrons (e⁻) and holes (h⁺), are produced at the photoanode as a result of intrinsic ionization caused by incoming photons (from sunshine).

ii. Basic Principle of EC water splitting

Electrolytic solution, electrodes are used in EC water splitting. When an electric potential is placed between the two electrodes, O₂ is produced at the negative electrode i.e. anode and H₂ is produced at the positive electrode i.e. cathode.^{20,41,42} Owing to the multiple steps and energy accumulation in each step, OER in the water splitting is catalytically stagnant and has a

significant overpotential when compared to the hydrogen evolution reaction. OER also has a strong dependence on the electrolyte's pH level because the results are different in alkaline and acidic media. The oxidation of two H₂O molecules in an alkaline or neutral solution results in the production of hydrogen and oxygen by depleting 0.404 V of potential. At a cost of 1.230 V, the hydroxyl group converted into oxygen and water in an alkaline medium (V Vs. RHE). This process runs more efficiently in an alkaline environment than an acidic one.⁴³

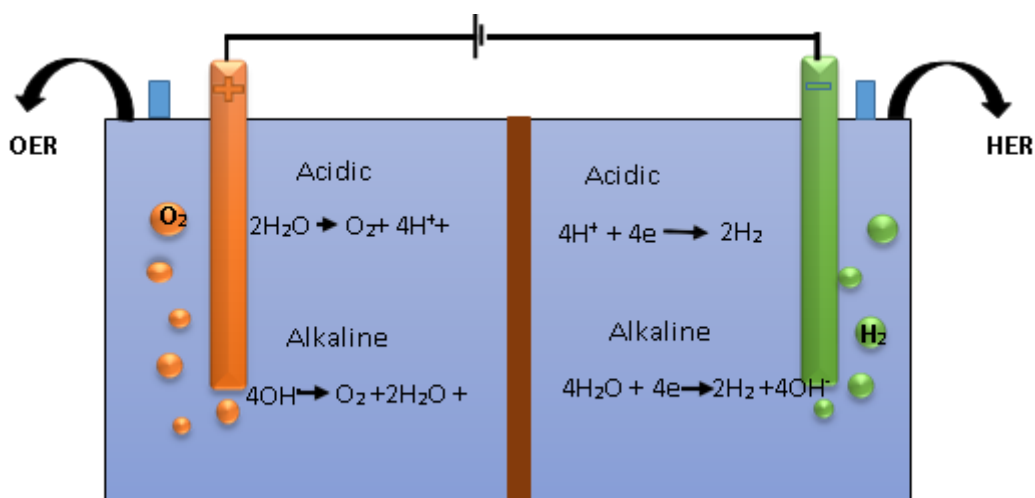


Figure 7: Mechanism of electrochemical water splitting

1.5. Research Objective:

The research objective is as follows:

- Preparation and analysis of Ni/Fe-MOF derived MOF/Fe₃O₄/NiO hybrid catalysts and Fe₃O₄/NiO-C
- Analysis of overpotentials of Ni/Fe-MOF, MOF/Fe₃O₄/NiO and Fe₃O₄/NiO-C.
- Analysis of applications of Ni/Fe-MOF, MOF/Fe₃O₄/NiO and Fe₃O₄/NiO-C. catalysts for HER, and OER and stability.

1.6. Scope of Study:

Producing hydrogen has a lot to offer Pakistan, a developing country with limited energy resources. Among many other uses, hydrogen is a resource that may be used as a fuel and energy source. Provided that it depends on water, a plentiful and common natural resource, the process' recurrent nature is a noteworthy benefit that will eventually guarantee a sustainable supply of hydrogen. Moreover, it is beneficial to use transition metals as catalysts in the process since it reduces reliance on rare and valuable metals, protecting against possible depletion. Water splitting creates hydrogen, but it also makes it possible to use it as a fuel for vehicles, a home fuel, and a crucial starting point for the synthesis of many other compounds, including ammonia.

Chapter 2

Literature Review

2.1. Literature Review:

The term "metal-organic frameworks," or MOFs, refers to porous crystalline solids with infinite lattices. For these solids, the name metal-organic frameworks (MOFs) is frequently employed.⁴⁴⁻⁴⁷ The development and use of MOFs were made possible in the 1990s by groundbreaking work done by research teams under the direction of Robson et al., Moore et al., Yaghi et al., Kitagawa et al., and Férey et al.⁴⁸. With more than 20,000 different MOF structures known, many of these structures are now easily accessible for purchase through a variety of distributors thanks to BASF's efforts in mass manufacture. Numerous industries, including oleo-chemicals, textiles, transportation, electric vehicle prototypes, food packaging, respiration systems, and chemical sensing, have discovered uses for these materials⁴⁹.

MOF materials can give high catalytic performance in the field of electrocatalysis and can construct hollow structures with controllable size and tunable morphology through an acceptable combination of organic ligands and metal centers. This allows for the formation of MOFs materials. In general, the surface areas of MOF materials are large, and these materials also have their own unique nanopore architectures. When it comes to boosting OER and ORR reactions, both qualities might be seen as beneficial. In addition, the production of significant quantities of N-doping as a byproduct of the pyrolysis of MOFs as precursors makes ORR and OER processes more likely to occur. These reactions have the potential to modify carbon material's electronic structure and generate active centers of M-N_x, both of which contribute to increase in number of bifunctional catalytic active sites in an efficient manner. Zeolite-imidazole framework, often known as ZIF, is one of the many different forms of MOFs that has been used widely in the development of bifunctional catalyst. This is due to the versatility of the framework as well as the usage of transition metals as the framework center. It is projected that ZIF-67 will be a potential candidate for the development of

bifunctional catalysts. This is because transition metal cobalt has remarkable catalytic capability for OER and ORR. Calcination and carbonization at a temperature of 700 degrees Celsius were necessary to manufacture nano-cobalt particles that were encased in nitrogen-doped polyhedrons that were produced with carbon nanotubes (MOF-CNTs). This process took place in an atmosphere that contained hydrogen and argon. In order to get this process started, Wu et al. used ZIF-67 (precursor)⁵⁰. MOF-CNTs displayed good electrocatalytic stability and activity in terms of OER and ORR. This may be owing to synergistic effect that is created when cobalt-rich nanoparticles are combined with CNTs. When measured against RuO₂ and Pt/C found in commercial products, the ORR and OER values of MOF-CNTs were shown to be superior. Both carbon nanotubes' structure, which is hollow, and carbon nanocages' structure, which is robust and porous, provided high-speed routes for the transport of electrolytes. The catalyst contained abundantly doped nitrogen atoms as well as confined nanoparticles of cobalt, both of which induced additional active site and accelerated electron transfer for OER and ORR respectively. The MOF-CNTs possessed superior pore structure, a excellent specific area, and a excellent degree of graphitization, all of which were helpful to the process of improving stability and activity of bifunctional catalyst. This was achieved by graphitizing MOF-CNTs to high degree. It is essential to bear in mind that the activity of the catalyst as well as its stability will be directly impacted by the particle size as well as metal is spread throughout the substance that was generated from ZIF. ZIFs' transmission of active substances, surface area, and ratio of active site can all be increased by use of a particle size that is more suited to the environment and has a distribution that is more uniform.

Recently, Li and colleagues have discovered a method that is effective in altering the size of Co nanoparticles that are included within ZIF materials. Graphitized carbonitride (gC₃N₄) and glucose (Glu) were both injected at the same time for the first time using this technology, which made it the first adjustment strategy⁵¹. During the pyrolysis of imidazole and cobalt ions, the incorporation of g-C₃N₄ and Glu has been shown to effectively reduce the size of both cobalt particles and polyhedron. This procedure results in production of nitrogen-doped graphite electrocatalysts and bifunctionally active carbon-supported cobalt nanoparticles. This is accomplished through the synthesis of bifunctionally active carbon-supported Co nanoparticle. This is accomplished by limiting ZIF-67's growth rate. In addition, incorporation of C₃N₄ has potential to encourage the development of bamboo carbon

nanotubes on surface of the polyhedron, which are then encapsulated by nano-cobalt particles. As a result of electrical interaction between metal nanoparticles and carbon nanotubes, it has been demonstrated that metal nanoparticles that have been enclosed in carbon nanotubes are able to increase effective catalyst activity. With this procedure, the ZIF-67 crystal size could be adjusted to range of 0.31-0.93 μm , while size of Co NP could be adjusted to range of 9.5-46.6 nm. Because of variables such as the smaller ZIF-67 polyhedra' even distribution, enhanced efficiency of active sites, and powerful Co-pyridyl-N coupling effect, catalyst displayed outstanding catalytic activity in both ORR and OER.

During the synthesis of ZIF-67, part of the cobalt in the precursor was replaced with zinc, which resulted in an improvement in the catalyst activity. Expulsion of zinc during high-temperature pyrolysis was found to be the cause of the observed improvement. This led to the creation of 21 catalysts with a porous structure and greatly enhanced specific surface area. This was accomplished by pyrolyzing the zinc at elevated temperature. Dispersion and size of cobalt nanoparticles were altered in the interim by adjusting ratio of zinc ions to cobalt ions in the precursor. This was done to prevent the cobalt particles from becoming clumped together during the process of catalysis. The pyrolysis of a bimetallic Co/ZnZIF mixture resulted in the production of carbon nanomaterials (porous). These porous carbon nanomaterials are porous and carbon nanotubes that were loaded with 14nm cobalt nanoparticles⁵². It was discovered that the catalytic efficacy was outstanding for both function of catalyst ($E_{j10}(\text{OER})-E_{1/2}(\text{ORR})=0.65\text{V}$) and exceptional long-term stability in both ORR and OER can be attributed to presence of numerous N-doped nanotubes, highly graphitized carbon, hierarchical mesoporous and microporous structures, as well as the uniform dispersion of nano-Co particles. In addition, this extraordinary long-term stability can also be due to presence of nano-Co particles.

Wang et al. were able to generate a highly effective bifunctional electro-catalyst with a core-shell structure by first subjecting ZIF-8@ZIF-67 to hydrothermal treatment and then carbonizing the mixture⁵³. They started by synthesizing ZIF-8 with just the zinc ion precursor in it. Because dimethylimidazole was present, it was simple to coordinate cobalt ions on surface of the crystals throughout the process of successfully fabricating core-shell structural ZIF-8@ZIF-67 crystals. The one-of-a-kind coreshell structure had the potential for

interactions that were synergistic, while also integrating the benefits of both ZIF-67 and ZIF-8. This might result in increased catalytic activity for oxygen release and oxygen reduction. It is possible to manufacture a variety of active centers inside the MOF material by including more than one metal in the synthesis process. These centers will have additive rather than additive effects. To boost OER catalytic activity, metallic nickel was typically included in the Co-MOF matrix in most cases. The bimetallic CoNi-MOF composite was used as precursor in Ning et al. preparation of porous Nitrogen-doped carbon coated CoNi alloy nanoparticle, which they referred to as CoNi@N-C⁵⁴. Altering the proportions of cobalt and nickel present in the precursor, as well as the temperature at which the pyrolysis was carried out, led to the discovery of the optimal ratio for the Co1Ni1@NC material. At the same time, the material displayed a distinct porosity along with a homogeneous distribution of CoNi alloy nanoparticles, significant quantity of 22 nitrogen atoms doping, and distributed active sites of CoNi-N_x. These characteristics suggested that the material might give remarkable catalytic activity in the OER and ORR processes. After pyrolysis, carbon polyhedron fell apart due to the weak binding force that existed between the organic ligands and the nickel, which served as a reminder to us that a more appropriate inclusion approach needs to be designed. Following the carbonization of MOF materials, a successful process for decorating additional metals has been established using adsorption or different methods. This is in addition to the strategy of directly introducing more metal ions into the precursor, which has proven to be effective. By modifying both pyrolysis temperature and quantity of Fe doped atoms, Pendashteh et al. were able to successfully produce a highly efficient electrocatalyst for ORR and OER. Co-ZIF-9 served the purpose of a sacrificial precursor. This resulted in the electrocatalyst having both ORR and OER functionality⁵⁵. Theoretical and experimental evidence demonstrated that adding Fe to a catalyst considerably enhanced its activity for OER and ORR by raising the total number of electrons transported.

It is possible to improve catalytic performance of bifunctional catalyst by employing a method that is both efficient and effective, and this opens the possibility of doing so. This method involves post-processing of materials that have been created from MOFs. By sulfiding, phosphating, selenizing, or oxidizing MOF materials, the authors of certain studies were able to produce good bifunctional catalytic activity. Co-sintering the catalyst with precursors like sulfur powder, selenium powder or sodium dihydrogen phosphate in the same heating

chamber at temperatures ranging from 200 to 450 degrees Celsius is the most typical method. These approaches, unfortunately, have the potential to disrupt morphology of material and induce structural collapse. This will influence the catalyst's surface area as well as transportation process, which will ultimately result in the MOF losing its activity.

To establish stable activity in MOF materials, it is necessary to address two important factors:

1. Taking use of synergistic impact that exists between active sites in MOF for ORR and OER.
2. Managing the subsequent treatment in such a way as to retain the integrity of the active sites that were present initially.

These two aspects are equally important to consider when trying to achieve a steady bifunctional activity in MOF materials. By accurately adjusting the level of Co-CN oxidation, Ding et al. were able to successfully manufacture a variety of Co-Co₃O₄-based nanostructures that were embedded in hollow N-doped carbon polyhedrons (HNCP). These nanostructures were embedded in carbon polyhedrons⁵⁶. They discovered that the length of calcination in an environment including O₂ and Ar had a discernible impact on morphology of both HNCP and Co-Co₃O₄. Co particles underwent a progressive transformation into Co/ Co₃O₄ with core-shell structure during the first step of calcination process. During the oxidation process, most of Co/ Co₃O₄-NP core shell transformed into Co@ Co₃O₄-NP yolk shell, and few Co₃O₄-NP hollow were produced. Bulk of Co@ Co₃O₄-NPs yolk shell in the Co₃O₄/HNCP-40 combination transformed into Co₃O₄ NPs hollow when the level of oxidation was increased even more, while part of structure of yolk shell remained intact. When the oxidation process was finished, the structure of egg yolk and shell was eventually transformed into hollow Co₃O₄ NPs. Fortunately, the level of oxidation could be well controlled, which resulted in the hollow carbon-based framework being kept in excellent condition. In the meantime, Co₃O₄/HNCP-40 yolk-shell displayed the greatest OER and ORR activity. It was due to multiple oxygen vacancies, additive effect of CoO and Co²⁺; the efficient mass transfer facilitated by the yolk shell and hollow N-doped carbon. This led to the ORR and OER dual function activity was best demonstrated by the yolk-shell combination of HNCP-40 and Co₃O₄.

Annealing treatment that is conducted on MOFs, the post-processing of MOFs consists of loading various catalytic particles onto MOF-derived materials. This is done in an effort to further increase the catalytic performance of the MOFs. To create porous $\text{Co}_3\text{O}_4@\text{ZIF-67}$ while maintaining outstanding activity, Li and his colleagues regulated oxidation level of ZIF-67. They did this by using a hydrothermal approach to evenly coat carbon shell surface with the CeO_2 nanoparticles⁵⁷. It was determined that the synergy between Co_3O_4 and CeO_2 was responsible for the catalyst's remarkable electrocatalytic bifunctional activity ($E_{j10}(\text{OER})-E_{1/2}(\text{ORR})=0.70\text{V}$), measured at electrode. Vacancies of oxygen on Co_3O_4 and CeO_2 boosted adsorption of oxygen on interface, accelerated activation of oxygen that was adsorbed to become oxygen O^{2-} and reduced lack of oxygen that was present during the ORR, which resulted in an improvement in the activity of the ORR. The contact between Co_3O_4 ($\text{CoOOH}/\text{Co}^{3+}$) and CeO_2 ($\text{Ce}^{4+}/\text{Ce}^{3+}$ and oxygen vacancies) provided the OER with access to additional electrochemically active sites, which considerably the smooth/generation transmission of active species (O_2 (O^{2-}) / O^-) and high charge transfer. Additionally, this interaction produced more active sites for OER. 24 MOF-derived materials are currently intensively explored in the field of electrocatalysis' advanced materials. This is primarily attributable to the controllability, modifiability, and versatility of MOF-derived-materials. This considerable investigation of materials generated from MOFs can in part be attributed to the remarkable traits and qualities of these materials. In the realm of MOF derived materials, the focus of study has mostly been on investigating the materials' catalytic activity for ORR. Comparatively little attention has been paid to determining the materials' electrocatalytic performance for OER. This dichotomy exists because the electrocatalytic performance of these materials for OER has not yet been deemed adequate. Directly integrating MOF materials that have strong ORR catalytic activity with extra components like Ni nanoparticles for increased OER catalysis. However, this strategy only produces a slight improvement and has a negative effect on the activity of ORR. The OER activity can be greatly increased with application of intensive oxidation or alternate calcination treatments; however, these treatments also result in a large reduction in the ORR activity.

This can happen even though the treatments can lead to excellent OER activity. To properly synthesize bifunctional oxygen catalysts, there are still a few areas that need additional research as well as improvements.

These areas are as follows:

- i) It is necessary to integrate the catalytic capabilities of OER and ORR while taking into consideration the synergistic effect that can occur between the active sites of both reactions to build bifunctional oxygen catalysts with any degree of success. This necessitates the development of novel synthesis procedures that can meet the bifunctional criterion in MOF-derived materials without relying on the external supplementation of the second catalytic function. Taking into full consideration synergistic effect between OER and ORR active sites.
- ii) Precisely regulating degree to which subsequent treatment is performed while simultaneously improving the electronic structure and morphology to achieve a balance between the catalytic activity required for ORR and OER.
- iii) Developing innovative synthesis methods that make most of the benefits of MOF materials and strike a healthy balance between catalytic activity and the inherent stability of the material. This is necessary to derive the most possible benefit from the use of MOF materials.

Through the introduction of intrinsic defects and the use of a fair quantity of heteroatom doping, metal-free carbon materials can give good dual-function electrocatalytic activity. Nevertheless, their catalytic performance, particularly their stability, has room for additional development. The serious corrosion of carbon at high voltage that occurs during the OER catalytic process will have a significant and negative impact on the life cycle of ZABs. In order to optimize performance of dual function catalysts and boost their stability, it is essential to incorporate a proper proportion of metal into materials based on carbon. Because of the numerous opportunities that lie ahead for them in the field of catalysis, single-atom catalysts, MOFs-derived materials, and graphene-supported materials have garnered great deal of attention⁵⁸⁻⁶⁰. Ever since graphene was discovered, its one-of-a-kind structure and performance have been the subject of extensive research. 2010 marked the year that the prestigious Nobel Prize in Physics was bestowed upon the researcher who was responsible for the discovery of graphene. Graphene has some remarkable properties, such as high carrier mobility of up to $10000 \text{ cm}^2 \text{ V}^{-1} \text{ s}^{-1}$, thermal conductivity ranging from $3000 \text{ to } 5000 \text{ W m}^{-1} \text{ K}^{-1}$ at ambient temperature, significant surface area of approximately $2630 \text{ m}^2 \text{ g}^{-1}$, an

exceptional optical transparency of around 97.3%, and an impressive mechanical strength with a Young's modulus of 1.0 TPa. Because of its remarkable material properties, graphene can perform both the role of a carrier for dual-function catalysts and the role of a catalyst on its own. These properties include great thermal and electrical conductivity as well as high specific surface area. A high-efficiency method for synthesis of composite catalyst has been contemplated, and it involves loading transition metal nanoparticles onto materials made of graphene. Because of the sequence in which transition metals are ranked in terms of their electrocatalytic activity, it might be difficult to fulfill the requirements for both the ORR and the OER. ORR activity order in electrocatalytic reactions goes as follows: Ni > Mn > Cu > Co > Fe, whereas the OER activity order goes as follows: Co > Cr > Zn > W > Ni > Fe/Cu/Mn > Mo. Because of this, it is difficult for single metal to satisfy prerequisites of both ORR and OER at same time. To solve this problem, it is necessary to use an alloy that is a blend of several different metals. This strategy is essential to solve the issue at hand in an efficient manner^{61,62}. It is possible to do what must be done by combining a heat reduction system with a 2-step sol-gel process, Khani et al. were able to synthesize a series of single metal nanoparticles consisting of iron, nickel, and cobalt as well as their ternary and binary alloys.

These nanoparticles were encased in a graphite carbon shell⁶³. Several different ex-situ characterizations suggested that the outermost layer of graphite had been electrochemically peeled away as a result of the extreme circumstances that were present during the electrochemical process. The electrically modified graphene inner layer did not flake and stayed unbroken, which effectively prevented the bulk of metal particles from taking part in the electrocatalysis process. This leads one to believe that some metal nanoparticles were not entirely encased by graphite shell, which resulted in the formation of an extra active site for electrocatalytic activity, particularly in the process of OER. As electrochemical reactions progressed, there was a corresponding increase in the concentration of metals near the surface of the sample that had higher oxidation state. This finding suggests that a fraction of the metal nanoparticles was not sufficiently encapsulated within graphite shell. This was demonstrated by the fact that the quantity of metal close to the surface that was in a highly oxidized state increased. Because of this, the performance of the Ni-Fe binary system was encouraging in terms of OER, whilst the performance of the Co-Fe binary system was the most successful in terms of ORR. Ternary alloys Ni-Co-Fe that are encased in graphite carbon shell (GNi_{1:3},

Co_{1.3}, Fe_{1.3}), which are manufactured by changing compound's metal ratio, have potential to both achieve an effective electrocatalysis which leads to practical MABs. This is because the compound is manufactured by changing compound metal ratio. In addition to the utilization of metal nanoparticles, loading graphene with transition metal hydroxides, sulfides, oxides, and nitrides is an additional effective technique for synthesis of bifunctional catalysts. In contrast to metal particles, metal compounds that have a greater valence have a lower probability of becoming oxidized, which results in a longer lifespan for the catalytic reaction that they catalyze. By exposing cobalt-containing precursors and graphene to pyrolysis in ammonia atmosphere at a temperature of 500 degrees Celsius, Zou et al. were able to successfully create interconnected amorphous cobalt nitride (Co-N_x) nanoparticles within a three-dimensional (3D) N-doped graphene aerogel (NGA)⁶⁴. Excellent catalytic performance was obtained by the Co-N_x-NGA for both ORR and OER ($E_{j_{10}(\text{OER})} - E_{1/2(\text{ORR})} = 0.6\text{V}$). This was made possible by the dual-active CoN_x and the hierarchically porous structure of the graphene aerogel. In addition to this, a different metal can be added to metal nitride, and atomic ratio of the two metals can be changed to improve electrocatalytic performance of catalyst. Researchers team headed by a scientist He Pyrolyzing matching graphene and metal hydroxide allowed him to make uniform and ultrafine Ni_x-Co_y-N nanoparticles that were anchored to N-doped reduced graphene (Ni_x-Co_yN/N-rGO)⁶⁵. An effective dual-function catalytic material was created when metal nitride uniformly dispersed was mixed with highly porous conductive N-rGO. By modifying metal atomic ratio, it was discovered that Ni_{2.25}Co_{0.75} N/N-rGO hybrid displayed higher durability and kinetic activity for both OER and ORR. This was the case even though the hybrid had lower atomic ratios of the two metals. In addition, Ni_{2.25}Co_{0.75} N/N-rGO electrocatalyst-assembled ZABs had a high value 193 mW cm⁻² (power density) and 864 W h kg⁻¹ (weight energy density). These batteries also exhibited a cycling capability up to 166 hours at current density of 10 mA cm⁻² and charge/discharge voltage gap of 0.72 V. In addition, incorporation of two distinct kinds of metals and compounds of metals enables each component to contribute to the activity of either ORR or OER. Furthermore, successfully combining the benefits that each offers as a means of building dual-function catalysts is yet another way to do this. On the other hand, simple mixing will lessen their intrinsic activity and might possibly have a negative effect on the ORR/OER performance.

The synergistic impact that might occur between several metal phases can significantly boost the activity of OER and ORR. Using sol-gel polymerization, Fu and his colleagues were able to develop Ni-MnO/rGO materials. These materials featured thin nanoparticles of Ni-MnO that were uniformly dispersed on a porous three-dimensional graphene network. MnO was determined to play the most important part in the ORR activity, whilst Ni was responsible for OER activity. Both components contributed to the overall activity⁶⁶. Remarkably, catalytic performance of Ni-MnO/rGO in a 0.1M solution of KOH topped that of any individual metal. The ORR half-wave potential ($E_{1/2}$) of Ni-MnO/rGO was measured at 0.78V, while the OER overpotential ($E_{j_{10}}$) was measured at 1.6V.

However, additional research is required in the area of the design of electrocatalysts that can perform two functions simultaneously. In fact, the method of integrating graphene materials by transition metals as a dual function catalyst for oxygen can also be applied to variety of other carbon-based materials such as carbon nanotubes, carbon nanosheets, and C_3N_4 , amongst others. This is because graphene is a two-dimensional material. This is because graphene is a two-dimensional material. Both ORR and OER can benefit from enhanced catalytic performance if the catalyst is doped with the appropriate heteroatoms and its specific surface area is modified. In a nutshell, graphene has been the subject of a significant amount of research as an innovative material over the past several years. Additionally, its application in the field of electrocatalysis has undergone significant development and improvement, whether it is used as catalytic species itself or as carrier. The fulfillment of diverse catalytic needs can be accomplished through incorporation of a wide variety of metal and compounds. Maximizing the catalytic effect can be accomplished by the efficient combination of the benefits offered by a wide variety of components. The most significant drawback of graphene supported catalysts, on the other hand, is that their bifunctional catalytic stability and activity are not yet on par with those of other cutting-edge materials.

Consideration should also be given to the following areas to concentrate on to make improvements:

- a) It is vital to develop innovative anchoring strategies that successfully hold the catalytic particles onto or within the graphene material to prevent the loss of activity and agglomeration of nanoparticles that occurs during the process of electrocatalysis. This

will allow for the prevention of the aggregation of nanoparticles. It is necessary to do this to keep the action going and stop the particles from clamping together.

- b) It is essential to develop efficient techniques of synthesis that can optimize the size of catalytic particles and promote a uniform dispersion throughout the material to make complete use of graphene materials. This will allow graphene to be utilized to its maximum potential. Graphene can be employed more effectively, leading to improved performance and increased usage of its capabilities, if an even dispersion of the material can be achieved.
- c) To achieve the goal of enhancing interaction between catalytic particles and the graphene substrate, a comprehensive inquiry is being carried out with the intention of conducting an in-depth analysis of combined catalytic effect of several distinct components. The purpose of this investigation is to gain a better knowledge of how the various components work together to contribute synergistically to the catalytic activity, which ultimately leads to an interface that is optimal between the particles and the graphene substrate

Table 1: Comparison of HER and OER activity for Ni-Fe-MOF, Fe₃O₄/NiO/Ni-Fe-MOF and Fe₃O₄/NiO-C electrocatalyst with other recently reported Fe and Ni based electrocatalysts.

Catalyst	J (mA/cm²)	Overpotential l HER (mV)	Tafel slope (mV dec⁻¹)	Overpotential al OER (mV)	Tafel slope (mV dec⁻¹)	Year	Ref
C/Ni- AuPt-3	10(HER)	161	76	-	-	2022	⁶⁷
FeC	10(HER) 10(OER)	435	221	510	154	2024	⁶⁸
Ag₂O/NiO	10 20	140 300	78	430	98	2024	⁶⁹
Ni- BTC/CC	10(HER) 10(OER)	441	213.2	390	114.2	2022	⁷⁰
Ni-Fe-MOF (12h)	10(HER) 50(OER)	150	134	362	-	2023	⁷¹
Fe₃O₄/ NiFeLDH/Fe ₃O₄	10(HER) 500(OER)	134	141.5	346	87.5	2023	⁷²
CoPn/NF	10(HER) 100(OER)	144	-	330	68	2020	⁷³

Fe₃O₄/	10(HER)	94	68	268	55	2022	⁷⁴
RuO₂-C	20(OER)						
NiO/	10(HER)	106	126	242	86	2024	⁷⁵
NiFe₂O₄	10(OER)						
Fe₃O₄/Ni	10(HER)	143	39	242	42	2023	⁷⁶
	10(OER)						
Ni-Fe-MOF	10(HER)	268	54.5	360	103	This	-
	100(OER)					work	
Fe₃O₄/NiO/	10(HER)	210	153	340	74	This	-
Ni-Fe-MOF	100(OER)					work	
Fe₃O₄/	10(HER)	147	53	240	59	This	-
NiO-C	100(OER)					work	

Chapter 3

Apparatus and Characterization Techniques

In this section, a brief discussion is provided about the equipment used throughout the experimental synthesis procedure of both MOFs and their composites. Afterward, all the necessary characterization techniques, including XRD, SEM, EDX, BET, FTIR, and LSV will be discussed. These techniques are used to analyze the structural, elemental, and electrochemical properties of the material.

Apparatus Required

The apparatus used during the experimental synthesis of MOFs and their composite are as follows:

- Digital balance,
- glass beakers,
- magnetic stirrer,
- Hotplate, Teflon beaker,
- pH papers,
- Petri dish,
- Sonicator,
- Centrifuge tubes, centrifuge machine,
- electric oven,
- safety gloves, parafilm, butter paper, micropipette, and droppers.

Digital weight balance

Digital weight balance is an electronic instrument used to precisely measure the mass of the samples.

Hotplate

Laboratory hot plates serve as a heating source to uniformly heat solutions and materials. The hot plate also contains a magnetic stirring system. It has a magnet inside of it, for mixing solution Paired with a magnetic stir bar.



Figure 8. Hot plate with a beaker containing blue solution.

Autoclave

For crystal growth under hydrothermal (aqueous) conditions, a specialized reaction vessel known as an autoclave is essential. In the hydrothermal method to synthesize inorganic materials for extended intervals (longer reaction time) highly corrosive salts are used. The autoclave, therefore, must be designed such that it sustains highly corrosive solvents for a very long time at high pressure and temperature. By selecting an appropriate autoclave, the primary and most vital parameter is the test pressure and temperature conditions and the resistance to corrosion at that temperature-pressure range in the given hydrothermal fluid (aqueous liquid). To prevent the decay of autoclave materials, it should be covered with nonreactive or inert materials (i.e., Teflon) from inside. Teflon has a large thermal expansion coefficient. It therefore expands and contracts more upon the heating and cooling cycle than its enclosed components.

Characteristics of an ideal hydrothermal autoclave

- a.** A perfect autoclave must be inert to acid, base, and oxidizing agents.
- b.** It should be capable of tolerating high pressure and temperature for a protracted time.
- c.** It should be easily assembled and disassembled.
- d.** And it should be long enough to induce the specified temperature gradient, etc.



Figure 9: Stainless steel autoclave with Teflon beaker generally used for solvothermal or hydrothermal synthesis

Electric Oven

Electric ovens are used for hydrothermal synthesis and drying of materials, it provides controlled and consistent heat for various experimental and sample preparation processes. Fig.10 shows a typical electric oven.



Figure 10: Electric oven with temperature ranges up to 400°C

Centrifuge machine

A centrifuge machine is used to separate components of a liquid mixture based on their density and sedimentation properties. The HERMLE 50 ml centrifuge machine operates on the principle of sedimentation. When subjected to centrifugal force, particles with higher density are forced to the bottom of the tube, leaving behind the supernatant, which is mostly the solvent of the solution-based substance with lower density. Fig. 11 is an image of centrifuge.



Figure 11: Centrifuge machine used for washing process after hydrothermal synthesis.

Characterization Techniques

To identify the structure, surface morphology, elemental analysis, functional group, surface area, and pore size of all the prepared samples are characterized by following characterization techniques.

- X-ray diffraction (XRD)
- Fourier Transform Infrared Spectroscopy (FT-IR)
- Scanning electron microscope (SEM)
- Energy Dispersive X-ray Spectroscopy (EDS)
- Transmission electron microscope (TEM)
- BET (surface area Analyzer)

X-ray Diffraction (XRD)

In the field of material science, X-ray diffraction stands out as a valuable technique for assessing crystal structure, phase purity, crystallite size, and recognizing a range of known and unknown compounds. It's a non-destructive method for analyzing materials. X-rays with a wavelength comparable to the size of an atom are directed onto the sample being examined. The crystal structure diffracts the rays, which are then detected by a detector positioned at an angle to the plane of incidence. The typical crystalline structure comprises stacked lattices, forming repeated 'unit cells' in a three-dimensional arrangement. Consequently, simultaneous diffraction from a set of planes may stem from the first, second, and third layers.

The diffracted radiation arising from the crystal structure, exhibiting both i) identical phase and ii) a wavelength variance in integral multiples of λ , has the potential for constructive overlap. However, this scenario needs to satisfy the following condition.

$$AB + BC = n\lambda \dots\dots\dots 1$$

Where n represents a whole number and λ stands for the wavelength, since $AB = BC = \text{Sin}\theta$, equation 1 can be expressed as:

$$2d\text{Sin}\theta = n\lambda \text{ (referred to as Bragg's equation)}$$

The specific directions that appear as dots on the spreading pattern are referred to as reflections. XRD patterns result from electromagnetic rays hitting a widely dispersed array. Diffraction images are created using electromagnetic rays because they have a wavelength (λ) that is roughly equivalent to the distance (d) between the crystals. Diffraction occurs only when Bragg's law satisfies the criteria for producing interference of planes with distance "d".



Figure 12. Image of XRD machine

Fourier Transform Infrared Spectroscopy (FT-IR)

Spectroscopy explores the interaction and behavior of light or electromagnetic radiation with matter. IR spectroscopy specifically entails directing infrared photons through a sample, where the sample absorbs some infrared light and transmits the rest. The resultant spectrum reveals the molecule's absorption and transmission characteristics, creating a distinctive molecular fingerprint. Like fingerprints, each molecule configuration generates a unique infrared spectrum, enabling diverse applications for IR spectroscopy. The IR spectrum of a material is like its unique fingerprint, displaying absorption peaks that correspond to the frequency of vibrations between the bonds of the atoms in the material. Since each substance is composed of a specific set of atoms,

no two compounds have the exact same IR spectrum. As a result, IR spectroscopy can be employed for the positive identification of various substances. Moreover, the intensity of the peaks in the spectrum offers insights into the quantity of material present.

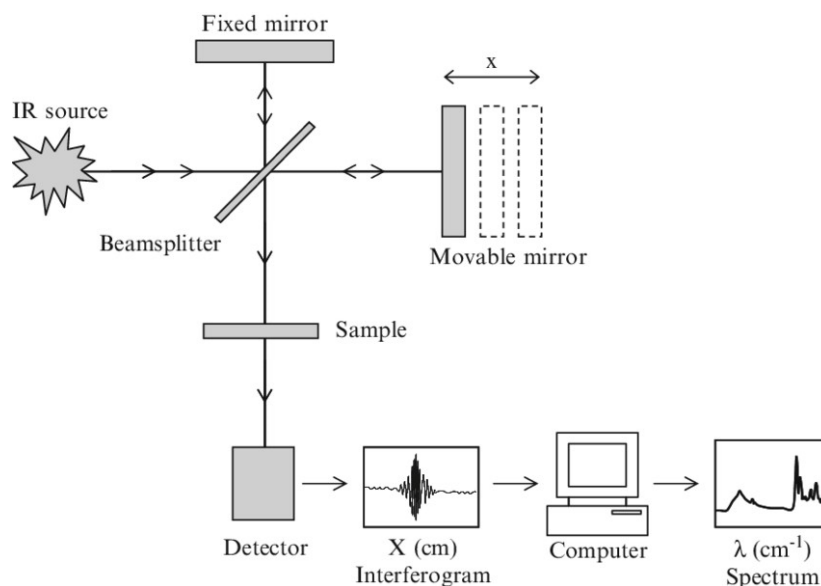


Figure 13: Working of FTIR spectrometer.⁹⁸

Scanning Electron Microscopy (SEM)

SEM is a type of electron microscope that gives the image of the sample by scanning it with a high-energy beam of electrons in a raster scan pattern. SEM gives the surface morphology of the materials and generates an electron beam within a vacuum. This beam undergoes collimation through electromagnetic condenser lenses, subsequent focusing via an objective lens, and then scanning across the sample using electromagnetic deflection coils. The primary imaging technique involves capturing secondary electrons (SE) released by the material. These electrons are revealed by a luminescent material that emits light flashes when hit by electrons. These flashes are then detected and amplified by a photomultiplier tube. By correlating the sample's scan position to the resultant signal, an image is generated, closely resembling what would be observed through an optical microscope. The resulting shadowing and illumination exhibit a natural-looking surface topology. In a Scanning Electron Microscope, the electron gun serves as the source for the probing

electron beams. Electrons are emitted from the cathode, accelerated through an electric field, and focused to form the primary image of the source. The apparent source's shape and size, beam acceleration, and current play pivotal roles in determining the SEM's performance and resolution. Typically, SEM offers magnification ranging from 20x to 30,000x with a special resolution of 50-100nm, enabling scanning of areas varying from one centimeter to five micrometers.^{77,78}

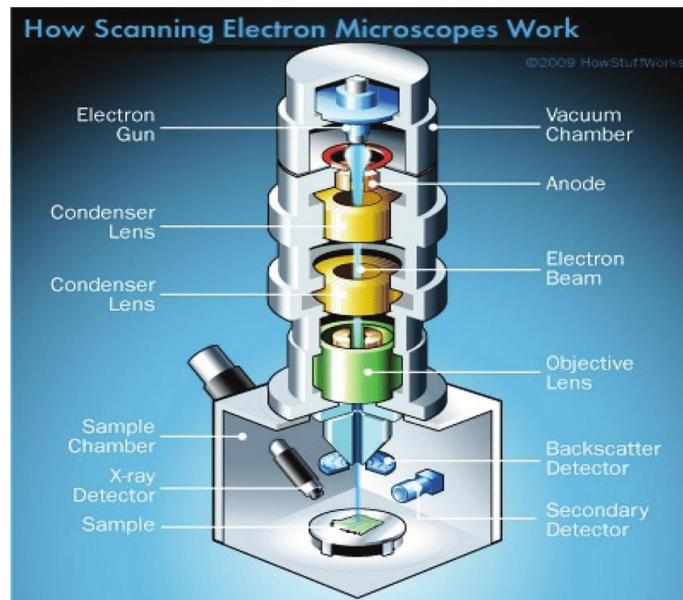


Figure 14: Schematic of working of Scanning electron microscope.⁷⁸

Energy Dispersive X-Ray Spectroscopy (EDX)

EDX analysis is used to determine the elemental composition of a material. It involves equipping an SEM instrument with an additional X-ray detector to collect radiation from the sample's internal part. In EDX analysis, a substantial amount of energy is necessary to enable the penetration of the sample by the electron beam. The interaction between the electron beam and the sample leads to the ejection of electrons from the lower shell (K and L) of the atoms, resulting in the creation of vacancies. To fill these vacancies, electrons from higher orbitals transition to lower orbitals, emitting X-ray radiation in the process. Inner shell transition from each element gives rise to characteristic energy value. By comparing the energy of the obtained X-ray with the known data

one can specify it to a known element. Fig. (15) represents the explanation of the phenomenon of EDX.

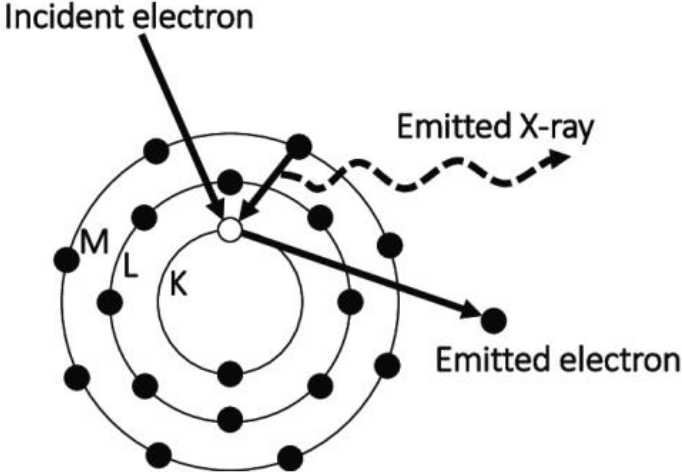


Figure 15: Schematic explaining EDX phenomenon¹⁰⁰

Chapter 4

Materials and Methods

Materials

Nickle chloride $\text{NiCl}_2 \cdot 6\text{H}_2\text{O}$, iron nitrate nano hydrate ($\text{Fe}(\text{NO}_3)_2 \cdot 9\text{H}_2\text{O}$) 1,4-Benzenedicarboxylic acid/terephthalic acid (H_2BDC), N, N Dimethylformamide (DMF), sodium hydroxide (NaOH), nefion, deionized water and ethanol were acquired from Sigma Aldrich and used without additional purification.

Synthesis

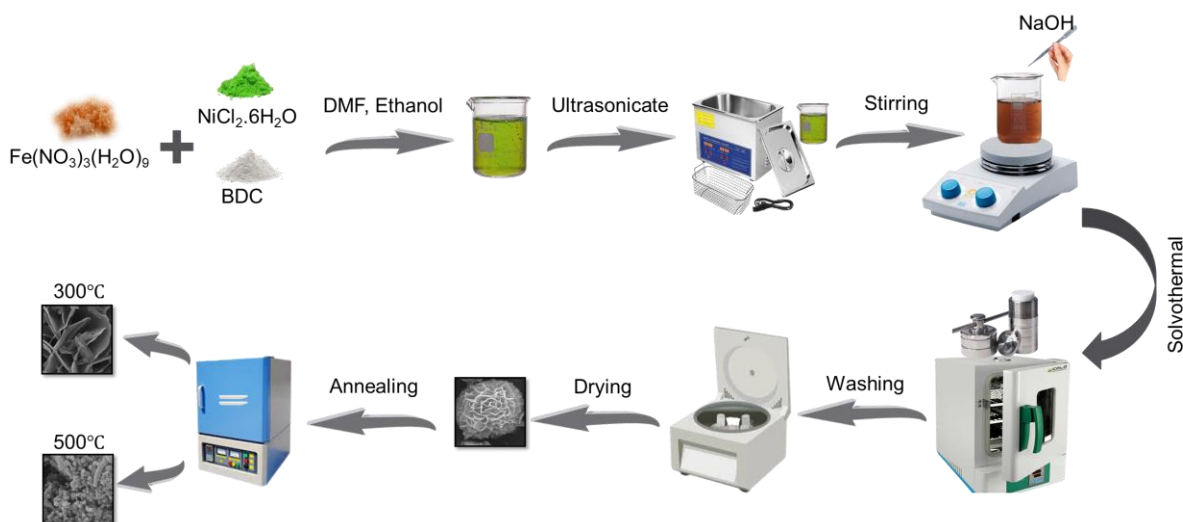


Figure 16: Synthesis Mechanism of Ni-Fe-MOF, $\text{Fe}_3\text{O}_4/\text{NiO}/\text{Ni-Fe-MOF}$ and $\text{Fe}_3\text{O}_4/\text{NiO-C}$

a. Synthesis of Ni-Fe MOF

Yun Luo and Xiaodong Yang's one-step hydrothermal technique synthesized Ni-Fe MOF with a small modification. Solution A was prepared by adding 3 mmol of BDC in 25 mL of N, N-dimethylformamide (DMF). Similarly, solution B was prepared by mixing 0.5 mmol of iron nitrate nano hydrate ($\text{Fe}(\text{NO}_3)_2 \cdot 9\text{H}_2\text{O}$) and 2.5 mmol of nickel chloride in 25 mL of ethanol solution. Sol A and Sol B were stirred separately for 5 minutes and

then mixed. The resulting solution was ultrasonicated for 15 minutes, followed by 25 minutes of stirring at room temperature. Subsequently, 2 mL of 0.4 M NaOH, dissolved in ethanol, was added dropwise into the above solution and stirred for 5 more minutes. The resulting mixture was transferred into a Teflon beaker and kept at 150 °C for 6 hours in an autoclave. The obtained product was washed multiple times with DMF and ethanol and dried at 60 °C for 24 hours in a vacuum oven.⁷⁹

b. Synthesis of Fe₃O₄/NiO-C

For the synthesis of Fe₃O₄/NiO-MOF and Fe₃O₄/NiO-C composites, the acquired greenish product was placed into two alumina crucibles and calcined separately at 300 °C and 500 °C in a muffle furnace for three hours. After calcination, the resulting product was allowed to cool naturally to room temperature. A brown powder was obtained for the sample annealed at 300 °C and blackish brown powder for 500 °C. Figure 16 shows the sequential steps of the synthesis process.

c. Synthesis Mechanism of Electrode for Water Splitting Using Nickel Foam

Materials:

Nickel foam (substrate)

Nefion (binder)

Ethanol(solvent)

Deionized water (for washing)

HCl (for washing)

Procedure:

Preparation of Nickel Foam Substrate:

- i. **Cleaning:** Nickel foam was cut into 1 cm x 1.5 cm dimension then cleaned it sonication in HCl (2-3 minutes), ethanol for 10 minutes, followed by deionized water for 10 minutes.*

- ii. **Drying:** Dry the cleaned nickel foam at 60°C in an oven or on hot plate for 2 hours.

Slurry of Catalyst

- i. **Preparation**

Take 2mg of catalyst powder and add 2 drops of nefion and 3 to 4 drops of ethanol in it. Sonicate the mixture for 30-40 minutes.

- ii. **Deposition:**

Take a micropipette and add slurry on the nickel foam by using micropipette in 1 cm x 1 cm dimension. Dry the foam at 60°C in an oven for 12 hours. Cover the dried nickel foam with butter paper and aluminum foil and press it with the weight of 500 N for 5sec.

Chapter 5

Results and Discussion

5.1. Characterization

The structural properties of Ni-Fe-MOF a bimetallic metal-organic framework along with its derivatives. $\text{Fe}_3\text{O}_4/\text{NiO}/\text{Ni-Fe-MOF}$ and $\text{Fe}_3\text{O}_4/\text{NiO-C}$ were evaluated using various techniques. X-ray diffraction (XRD) was used to examine the impact of annealing on crystal structures of Ni-Fe-MOF. Thermogravimetric analysis (TGA) was carried out for a quantitative assessment of the conversion of Ni-Fe-MOF into $\text{Fe}_3\text{O}_4/\text{NiO-C}$. Fourier transform infrared spectroscopy (FTIR) was employed to identify the functional groups in the Ni-Fe-MOF and its derivatives. Brunauer-Emmett-Teller (BET) analysis measured the surface area, pore size, and pore volume. Scanning electron microscopy (SEM) and energy-dispersive X-ray spectroscopy (EDX) were utilized to observe the surface morphology and elemental analysis respectively. To further investigate the internal structural properties transmission electron microscopy (TEM) was utilized.

5.1.1. X-ray diffraction (XRD)

X-ray diffraction (XRD) technique used to examine the structural properties of Ni-Fe-MOF and effect of annealing on the X-ray diffraction pattern of Ni-Fe-MOF. The XRD pattern of all the samples shown in Fig. 17 for as-synthesized Ni-Fe-MOF, $\text{Fe}_3\text{O}_4/\text{NiO}/\text{Ni-Fe-MOF}$, and $\text{Fe}_3\text{O}_4/\text{NiO-C}$. XRD of Ni-Fe MOF shows peaks at 2θ values of 8.8° , 10.4° , 15.7° , and 17.2° , indicative of its crystalline structure. The peak at 8.8° 2θ value, represents Fe-MOF and Ni- MOF, while peaks at 10.4° , and 17.2° , are like those previously reported for Fe-MOF (Fe3-MIL-88B) and peak at 15.7° and 18.0° reflect the planes of pure Ni-MOF.⁸⁰⁻⁸² $\text{Fe}_3\text{O}_4/\text{NiO}/\text{Ni-Fe-MOF}$ obtained because of annealing at 300°C shows an overlapped peak of Iron oxide (Fe_3O_4) and Nickel oxide (NiO) at 43° along with its pristine Ni-Fe-MOF's peaks at 2θ value of 8.8° , 15.7° and 17.2° . This presence confirms the formation $\text{Fe}_3\text{O}_4/\text{NiO}/\text{Ni-Fe-MOF}$ nanocomposite. As a result of the carbonization of organic ligands, a broad carbon peak at 20° 2θ value appeared after pyrolysis of Ni-Fe-MOF at 500°C .⁸³ Moreover, the

diffraction peaks at 37.25° , 43.28° , 62.86° , 75.39° , and 79.39° belongs to the crystallographic planes (111), (200), (220), (311) and (222) (JCPDS card no. 04-0835) of NiO respectively⁸⁴ and the diffraction peaks at 35.45° , 43.08° and 62.65° represents (311), (400) and (440) plane of Fe_3O_4 (JCPDS card no-01-1111).⁸⁵ The disintegration of the organic ligands at 500°C resulted in absence of Ni-Fe-MOF diffraction peaks indicates the complete conversion of MOF into respective oxides. To check the stability and durability of $\text{Fe}_3\text{O}_4/\text{NiO}-\text{C}$, XRD analysis was also performed after electrochemical stability testing and results are shown in Fig. 18 indicating its structural durability.

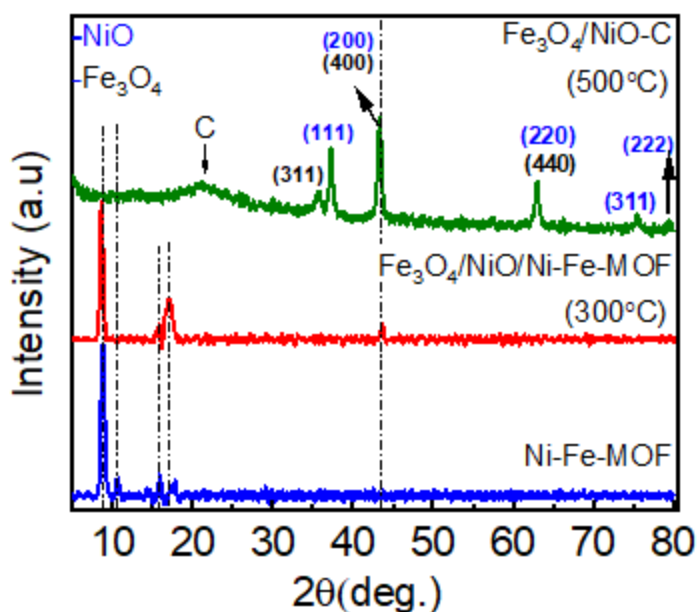


Figure 17: XRD pattern of pure Ni-Fe-MOF, $\text{Fe}_3\text{O}_4/\text{NiO}/\text{Ni-Fe-MOF}$ and $\text{Fe}_3\text{O}_4/\text{NiO}-\text{C}$

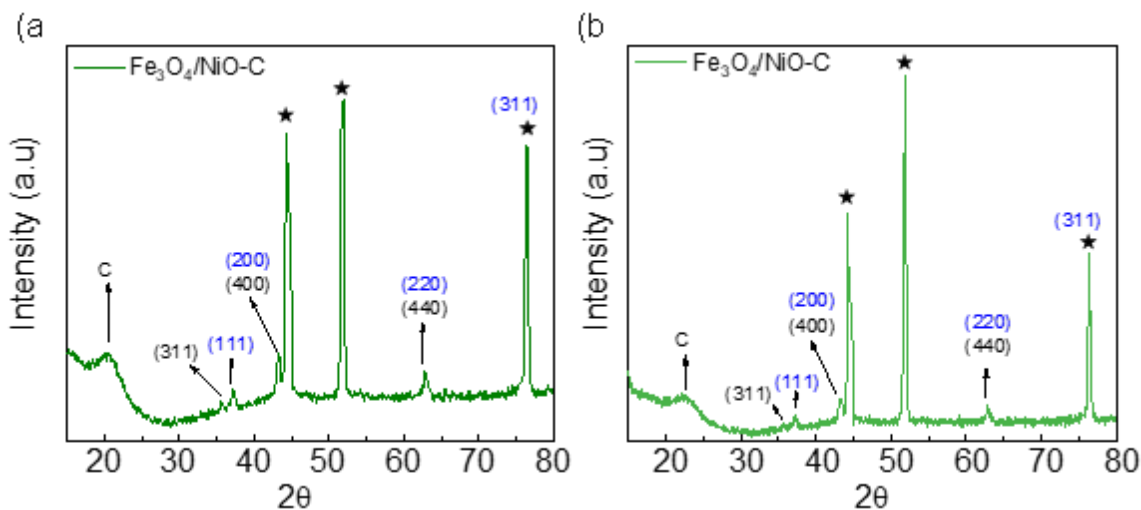


Figure 18: XRD pattern of $\text{Fe}_3\text{O}_4/\text{NiO-C}$ after 24 hours chronoamperometry test (a)OER and (b)HER

5.1.2. Thermogravimetric Analysis (TGA)

MOF conversion into oxides was further confirmed through thermogravimetric Analysis (TGA) as shown in Fig. 19. At 300 °C, only 16% of initial weight was reduced because of slight conversion of Ni-Fe-MOF into respective oxides. A sharp weight loss (61%) was observed at the temperature of 478 °C indicating the significant

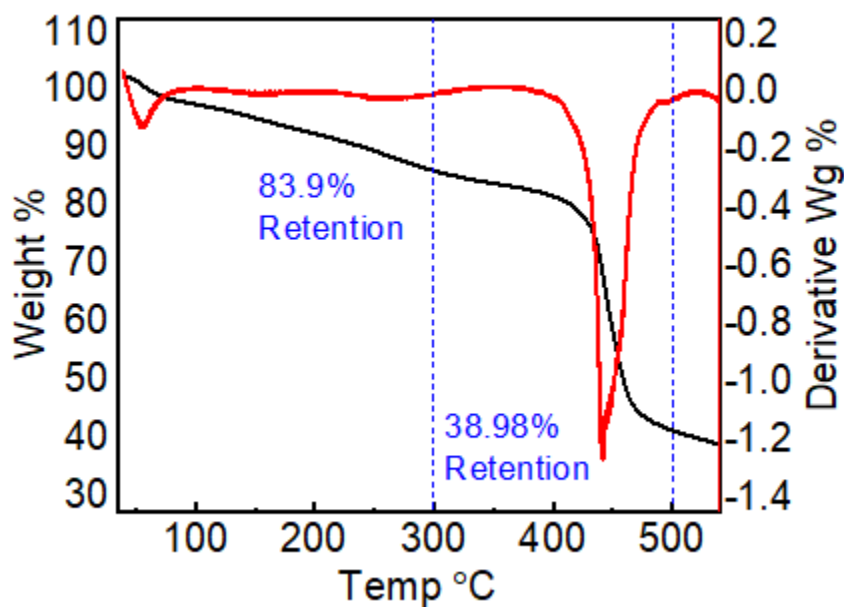


Figure 19: Thermogravimetric analysis of Ni-Fe-MOF, $\text{Fe}_3\text{O}_4/\text{NiO}/\text{Ni-Fe-MOF}$ and $\text{Fe}_3\text{O}_4/\text{NiO-C}$

disintegration of the MOF structure and conversion into oxides. To check the stability and durability of Fe₃O₄/NiO-C, XRD analysis was also performed after electrochemical stability testing and results are shown in Fig. S1 indicating its structural durability.

5.1.3. Fourier-transform infrared FTIR

The changes in the chemical composition because of annealing at different temperatures were also studied using Fourier-transform infrared (FTIR). The results are shown in Fig. 20. The fingerprint region of all the samples shows a peak around 540 cm⁻¹, indicating the presence of Fe-O and Ni-O bond. However, the shifting of this peak towards higher wavenumber because of annealing implies a relatively stronger bonding of metal ions with oxygen in the annealed samples. Ni-Fe-MOF and Fe₃O₄/NiO/Ni-Fe-MOF showed peaks around 750 cm⁻¹, 1398 cm⁻¹, 1573 cm⁻¹ exhibiting the presence of C-H asymmetric and symmetric vibrations of COO⁻ bonds, respectively, present in the molecular structure of BDC. The peaks associated with BDC were significantly reduced in Fe₃O₄/NiO-C due the disintegration of BDC at 500 °C. A broad band around 3430 cm⁻¹ was observed in all the samples suggesting their hygroscopic nature. Two sharp peaks around 3524 cm⁻¹ and 3588 cm⁻¹ in Ni-Fe-MOF and Fe₃O₄/NiO/Ni-Fe-MOF correspond to the O-H group present in BDC. These results suggest

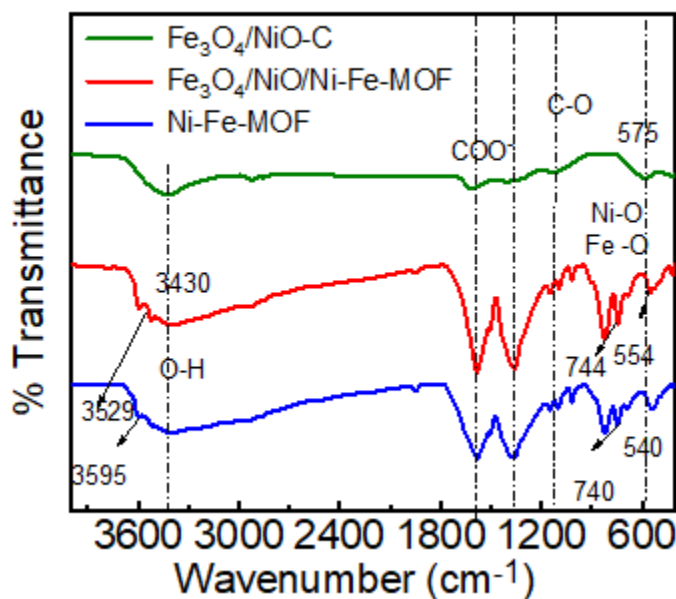


Figure 20 : FTIR spectra of all the synthesized sample Ni-Fe-MOF, Fe₃O₄/NiO/Ni-Fe-MOF and Fe₃O₄/NiO-C

annealing of Ni-Fe-MOF in air at 500 °C led to the significant conversion MOF into Fe₃O₄ and NiO, however, when the annealing temperature was low (300 °C) a partial conversion of MOF resulted in a composite of Fe₃O₄, NiO and Ni-Fe-MOF. ⁸⁶⁻⁸⁸

5.1.4. Vibrating Sample Magnetometer (VSM)

The magnetic behavior of synthesized Ni-Fe-MOF, Fe₃O₄/NiO/Ni-Fe-MOF and Fe₃O₄/NiO-C was analyzed by employing vibrating sample magnetometer. Fig 21 depicts all the samples' magnetic behavior. Ni-Fe-MOF and Fe₃O₄/NiO/Ni-Fe-MOF exhibit paramagnetic behavior due to organic linker (BDC). Whereas Fe₃O₄/NiO-C forms a hysteresis loop with a coercivity value of 113.58 A/m, indicating its soft magnetic nature. The soft magnetic nature of the MOF derived Fe₃O₄/NiO-C is in accordance with the hydrothermally synthesized Fe₃O₄@NiO reported previously in literature. ^{89,90}

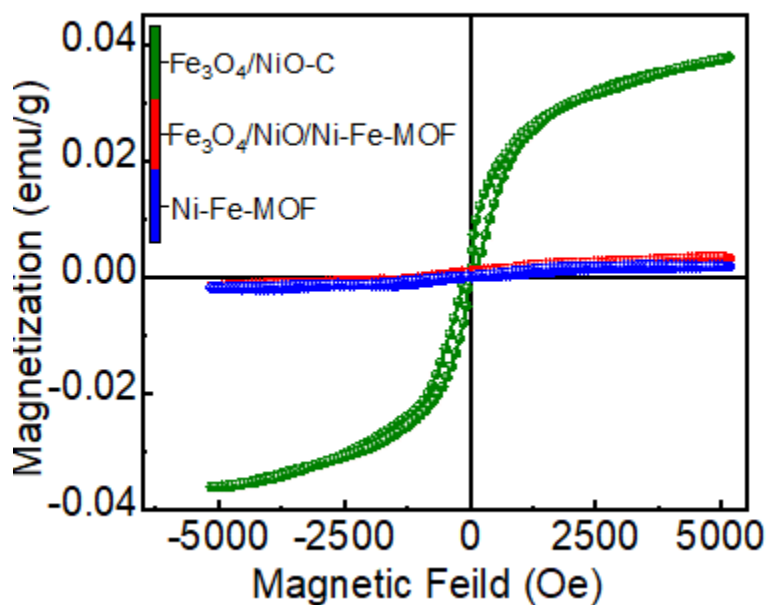


Figure 21: VSM graph of Ni-Fe-MOF, Fe₃O₄/NiO/Ni-Fe-MOF and Fe₃O₄/NiO-C

5.1.5. Brunauer, Emmett and Teller (BET)

The nitrogen adsorption/desorption technique was utilized to examine the surface area and pore size of all the three samples shown in Fig. 22(a-d). BET surface area, pore volume and pore sizes of all the samples are shown in Table 2. The surface area for Ni-Fe-MOF, $\text{Fe}_3\text{O}_4/\text{NiO}/\text{Ni-Fe-MOF}$ and $\text{Fe}_3\text{O}_4/\text{NiO}/\text{C}$ was obtained to be $79.9 \text{ m}^2/\text{g}$, $50.8 \text{ m}^2/\text{g}$ and $84.3 \text{ m}^2/\text{g}$, respectively. BJH pore diameter of these samples lies between 1.7000 nm and 300.0000 nm . The maximum surface area and pore size of bimetallic oxide $\text{Fe}_3\text{O}_4/\text{NiO}/\text{C}$ nanocomposite implies that converting MOF into oxides increases the surface area, pore volume, and size. The isotherms of all the samples show a complete loop over a large relative pressure range of $0.45 - 1$, indicating a conventional kind IV curve with an H3 hysteresis loop. The type IV route of isotherms is attributed to monolayer-

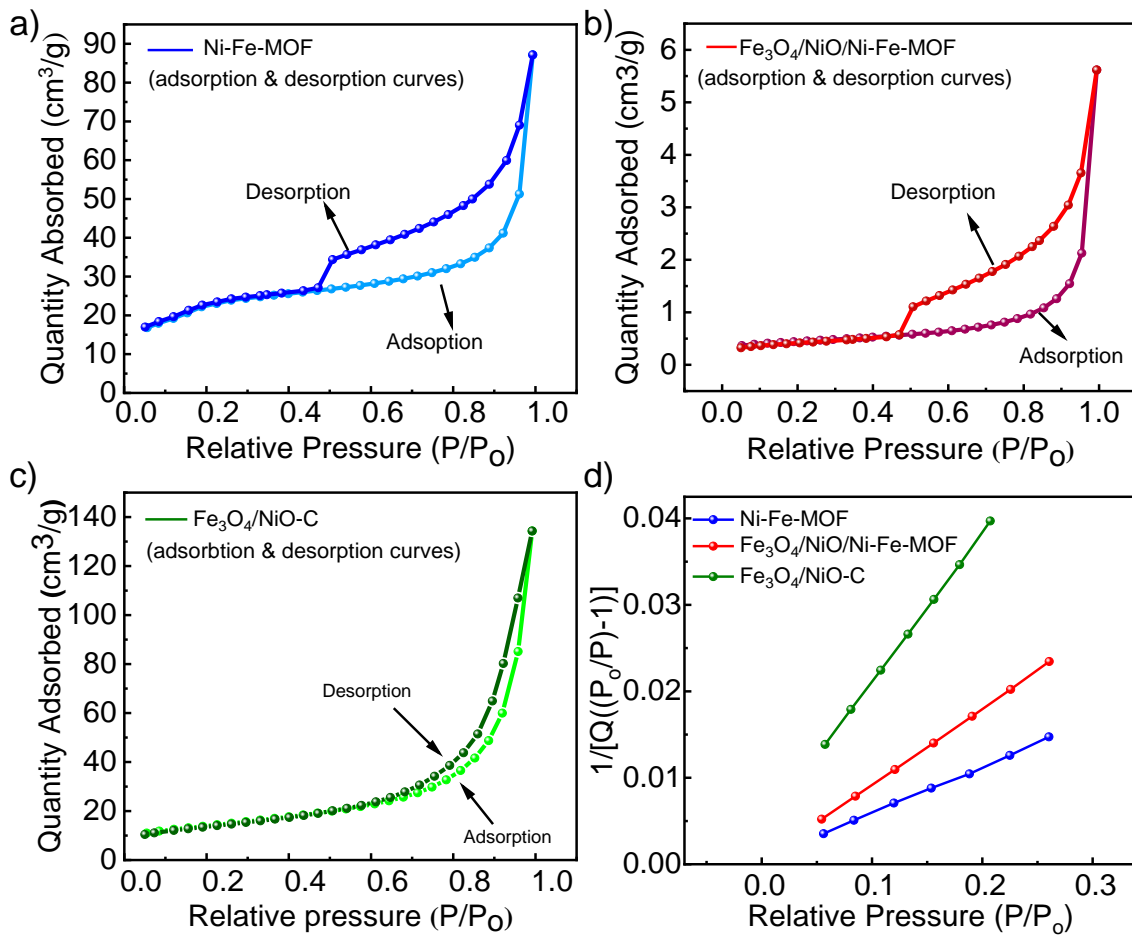


Figure 22: (a-d) Specific surface area and porosity of Ni-Fe-MOF, $\text{Fe}_3\text{O}_4/\text{NiO}/\text{Ni-Fe-MOF}$ and $\text{Fe}_3\text{O}_4/\text{NiO}/\text{C}$ was studied through BET analysis

multilayer adsorption while H3 hysteresis discloses the formation of slit-shaped pores. The desorption for kind H3 hysteresis includes a sharp section corresponding to the closure of the hysteresis loop owing to the tensile strength influence that occurs for nitrogen over a P/P₀.

Table 2 : BET surface area pore volume and pore size of Ni-Fe-MOF, Fe₃O₄/NiO/Ni-Fe-MOF and Fe₃O₄/NiO-C

Sample	BET surface area m ² g ⁻¹	Pore volume cm ³ g ⁻¹	BJH Pore size (nm)
(a)Ni-Fe-MOF	79.924	0.123	9.296
(b)Fe ₃ O ₄ /NiO/Ni-Fe-MOF	50.852	0.204	18.957
(c)Fe ₃ O ₄ /NiO-C	84.308	0.288	13.672

5.1.6. Scanning electron microscopy (SEM)

Scanning electron microscopy (SEM) was performed to analyze the morphology of Fe-Ni-MOF, Fe₃O₄/NiO/Ni-Fe-MOF and Fe₃O₄/NiO-C. The micrographs of these samples are shown in Fig. 23(a-f). Ni-Fe-MOF exhibits flower like morphology with 2D petals indicating porous nature of its particles. The SEM micrograph of Fe₃O₄/NiO/Ni-Fe-MOF shows that the pyrolysis at 300 °C has introduced irregularities in the smooth flower like morphology of Ni-Fe-MOF which can be easily observed by withered-looking petals in this samples, indicated by arrows. Moreover, the morphological characteristic of Ni-Fe-MOF is prominent in this sample indicating the slight conversion of the MOF into Fe₃O₄ and NiO which is also revealed by XRD results. The flower like morphology of the Ni-Fe-MOF was destroyed when the pyrolysis at 500 °C was carried out. The SEM images show agglomerated spherical-shaped nanoparticles of Fe₃O₄/NiO-C composite.

The porous morphology along with smaller particle size resulted in larger surface area in this sample as evidenced by the BET analysis. To evaluate the structural stability of Fe₃O₄/NiO-C SEM was performed after chronoamperometry for OER and HER and the results are shown in Fig. 24. It can be observed that the particles are still present some of them are agglomerated but with slight distortion the sample Fe₃O₄/NiO-C has retained its structure even after 24 hours of chronoamperometry test. These results indicate that the morphology of Fe₃O₄/NiO-C electrocatalysts is still maintained after the stability but with slight distortion.

The morphology of MOF reduced Fe₃O₄/NiO-C was further analyzed by TEM and the results are shown in Fig. 23(g-i). Fig. 23(g) shows TEM image of Fe₃O₄/NiO-C indicating the interlinked spherical shaped particles. Fig. 23(h) reveals the overlapping of NiO and Fe₃O₄ particles, confirmed by their respective interplanar spacings, indicating the interfacial interaction of nickel and iron oxide in this sample. Selected area electron diffraction pattern (SAED) of Fe₃O₄/NiO-C is presented in Fig. 23(i), ring pattern with bright diffraction spots demonstrating the polycrystalline nature of Fe₃O₄/NiO-C. Furthermore, the interplanar spacing of 1.4 Å, 2.01 Å corresponds to crystallographic planes (220) and (200) of NiO, respectively. Similarly, interplanar spacing of 2.36 Å and 2.5 Å corresponds to (222) and (311) planes of Fe₃O₄ respectively. XRD results also showed the presence of these planes in Fe₃O₄/NiO-C. To study the elemental composition of Fe-Ni-MOF, Fe₃O₄/NiO/Ni-Fe-MOF and Fe₃O₄/NiO-C

Energy-dispersive X-ray spectroscopy (EDX) mapping is a powerful technique used to analyze the elemental composition and distribution within a sample. EDX was performed for all the samples before chronoamperometry test and the results along with the colored mapping of elements are shown in Fig. 25(a-c). C, O, Ni and Fe are detected in Ni-Fe-MOF, Fe₃O₄/NiO /Ni-

Fe-MOF and Fe₃O₄/NiO-C their weight percentages are shown in the tables inserted in Fig. 25a, 25b & 25c respectively.

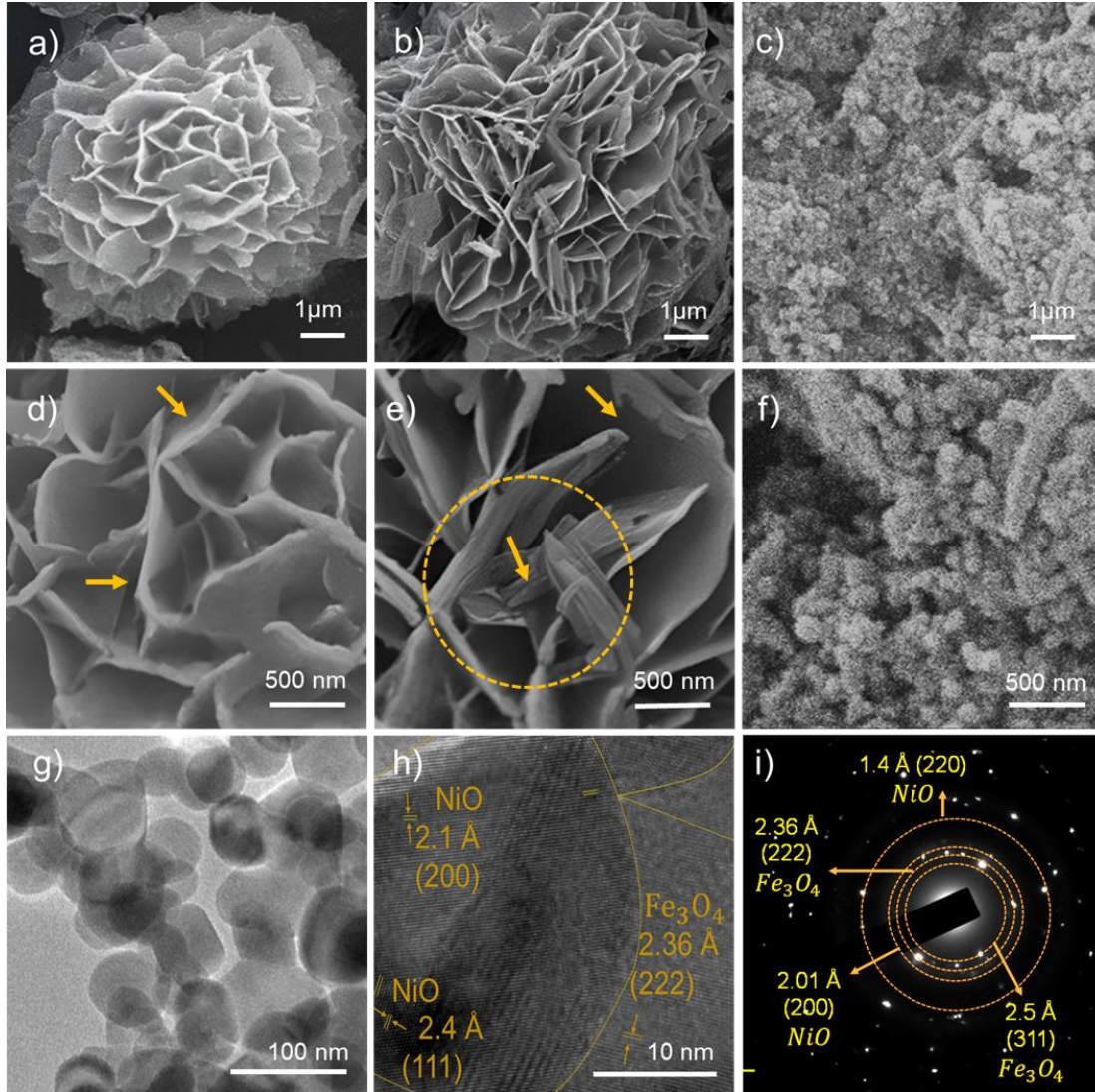


Figure 23:(a-f) SEM images of Ni-Fe MOF, Fe₃O₄/NiO/Ni-Fe-MOF and Fe₃O₄/NiO-C: (a) Ni-Fe-MOF showed flower like morphology with intricate 2D petals indicating its high surface area; (b) the pyrolysis of Ni-Fe-MOF at 300 °C resulted in the destruction of these petals like structure, however, the similarity of the morphology with Ni-Fe-MOF reveals abundance of the Ni-Fe-MOF in this sample; (c) depicts the complete distortion of flower like morphology and formation of agglomerated spherical particle with larger surface area in response to annealing at 500 °C. (g-h) TEM images further confirm the interlinked spherical particles of iron and nickel oxide in Fe₃O₄/NiO-C, along with (i) SAED patterns confirming the presence of Fe₃O₄ and NiO in the nanocomposite.

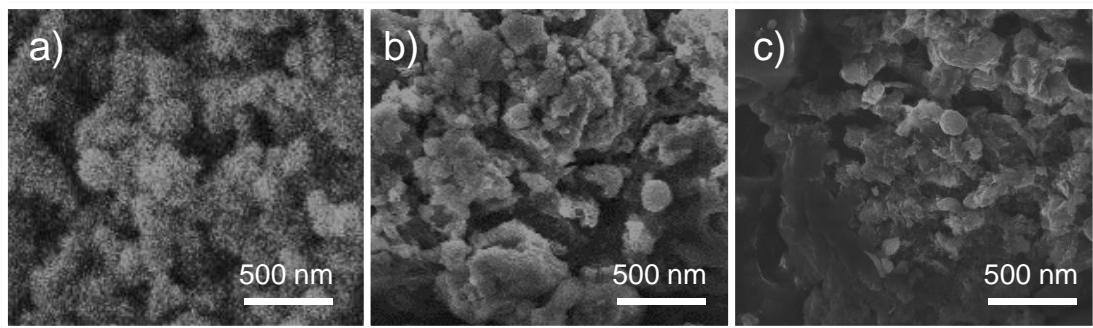


Figure 25: SEM images of $\text{Fe}_3\text{O}_4/\text{NiO}-\text{C}$ (a) before chronoamperometry, (b) after OER chronoamperometry, (c) after HER chronoamperometry.

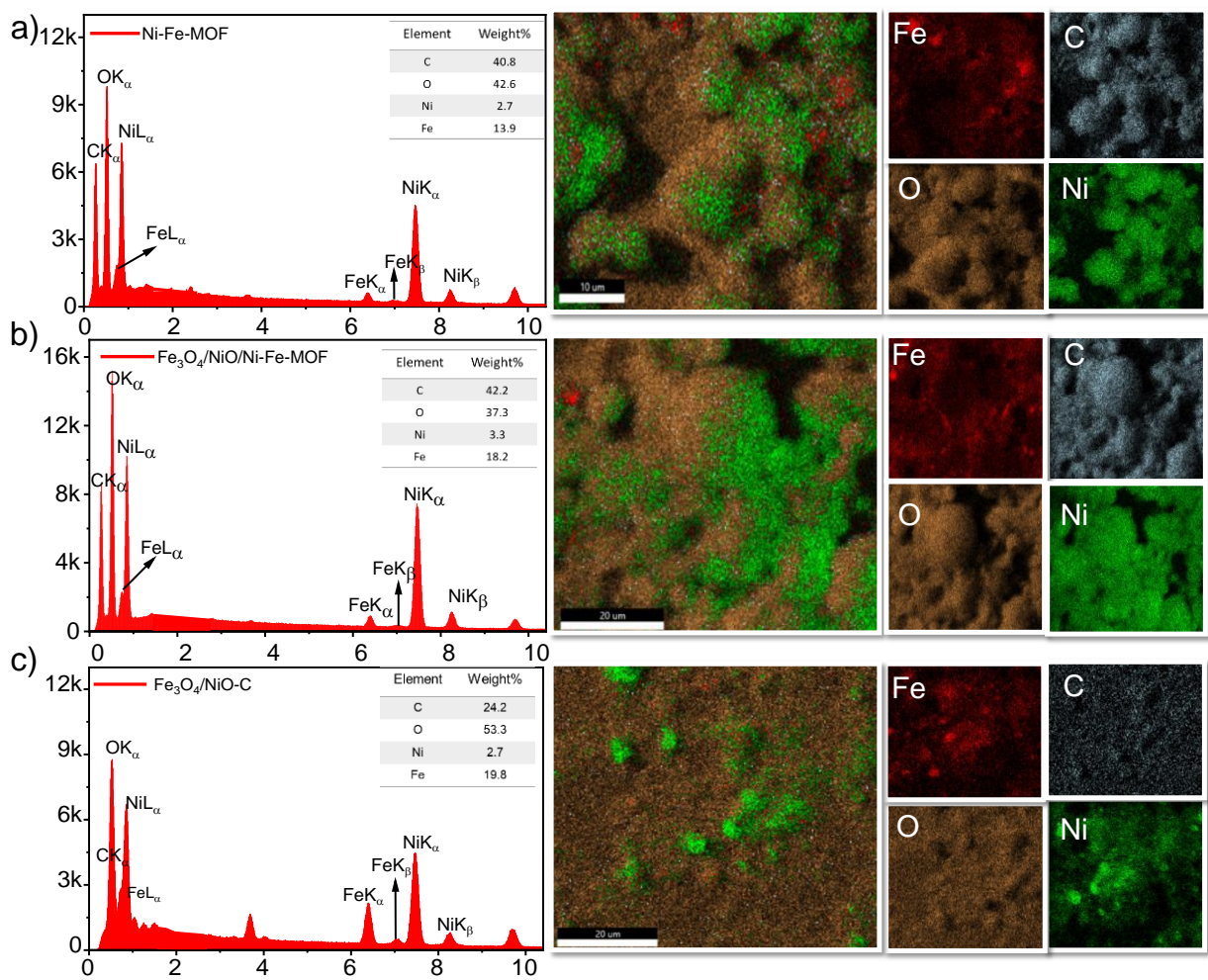


Figure 24:(a-c) EDX with color mapping confirming the presence of elements (C, O, Fe and Ni) in all the three samples (Ni-Fe-MOF, $\text{Fe}_3\text{O}_4/\text{NiO}/\text{Ni-Fe-MOF}$ and $\text{Fe}_3\text{O}_4/\text{NiO}-\text{C}$).

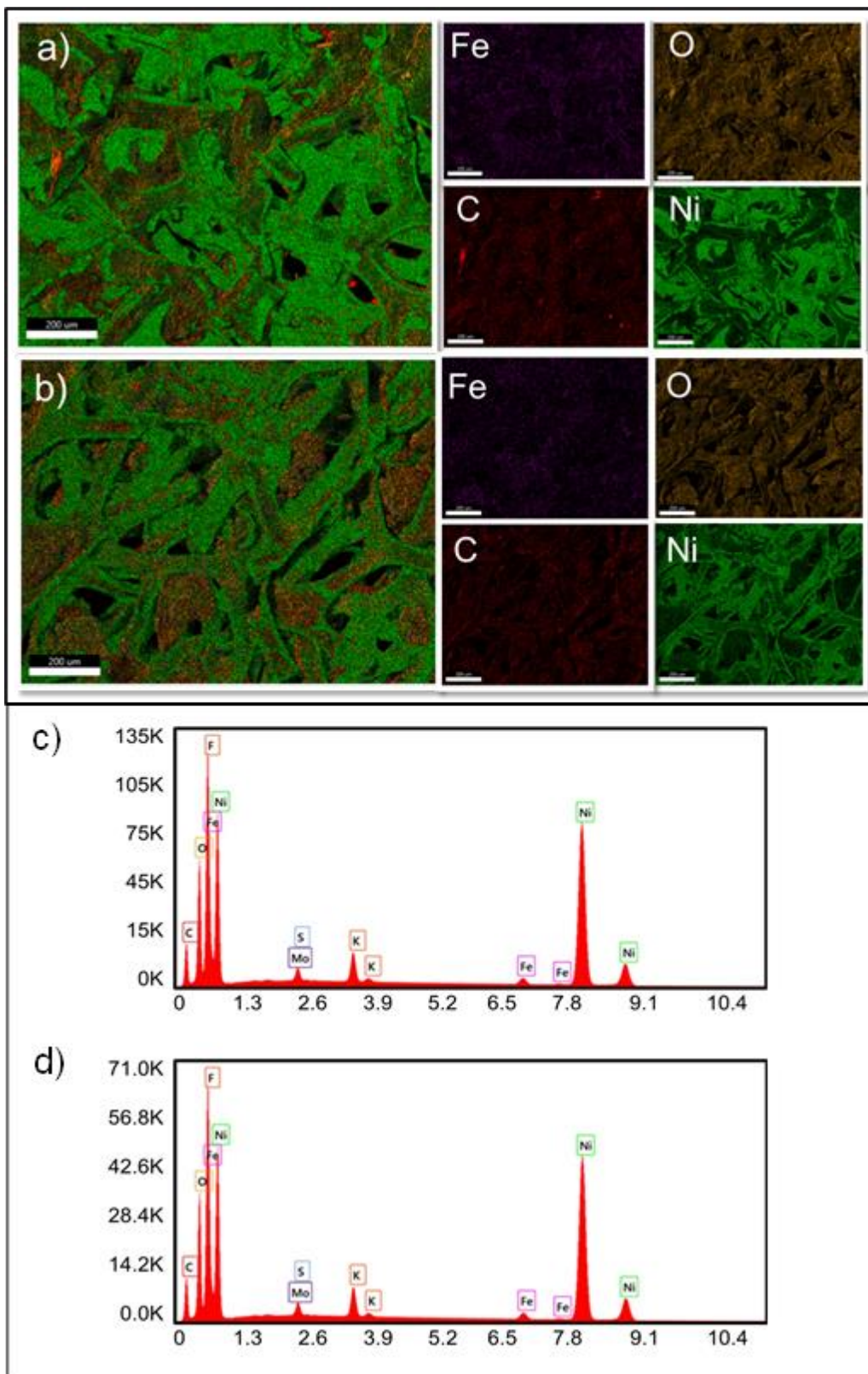


Figure 26: EDX graphs and mapping of $\text{Fe}_3\text{O}_4/\text{NiO-C}$ after OER and OER stability (a, c) after OER chronoamperometry (b, d) after HER chronoamperometry

Fig 26 (a-d) showcasing the results of EDS performed after chronoamperometry test (4a&4c (OER) and 4b&4d (HER)). The structural stability was evidenced by the presence of all the elements in Fe₃O₄/NiO -C even after stability test. The weight percentage of Ni was found to be the highest because of the Ni foam used as an electrode for our catalyst material.

5.2. Electrochemical Analysis

The electrocatalytic performance of all the samples Ni-Fe-MOF, Fe₃O₄/NiO/Ni-Fe-MOF and Fe₃O₄/NiO-C electrodes for both the hydrogen evolution reaction (HER) and the oxygen evolution reaction (OER) were assessed in 1 M potassium hydroxide (KOH) aqueous electrolyte solution. Electrochemical testing was conducted using a conventional three-electrode cell setup (potentiostat) at room temperature. All the electrodes were fabricated by depositing 2 mg of the synthesized electrocatalysts with nafion as a binder onto Nickel foam (NF), which served as the working electrodes. Platinum wire was used as a counter electrode, whereas the reference electrode was Ag/AgCl. All the potentials were converted to reversible hydrogen electrodes (RHE) by using the formula: $E \text{ (RHE)} = E \text{ (Ag/AgCl)} + 0.059 \times \text{pH}$. The overpotentials were adjusted for IR compensation.^{91,92}

Electrochemical performance of the synthesized electrocatalyst deposited on nickel foam were evaluated using linear sweep voltammetry (LSV). Fig. 27(a) shows oxygen evolution LSV curve at a scan rate of 10 mV/s of the prepared electrodes, illustrating the overpotential of all the samples calculated at current density of 100 mA/cm² and 500 mA/cm². The Tafel slope are shown in Fig. 27(b). Ni-Fe MOF showed an overpotential of 360 mV at 100 mA/cm² with a Tafel slope of 103 mV/dec, moreover, an ultrahigh current density of 500 mA/cm² was achieved at the overpotential of 500 mV. The low overpotential and reasonable reaction kinetics makes it to be a good electrocatalyst. The conversion of Ni-Fe-MOF into NiO/Fe₃O₄/Ni-Fe-MOF led to reduction in the overpotential value of the pure MOF to 340 mV with a reduced Tafel slope of 73 mV/dec at 100 mA cm⁻². The slight conversion of MOF into the NiO and Fe₃O₄ in this sample improved the overall performance due to the synergistic effect between NiO, Fe₃O₄ and Ni-Fe MOF as confirmed by XRD and TGA. The complete transformation of Ni-Fe-MOF into NiO, Fe₃O₄, and carbon exhibited a remarkable boost in the electrocatalytic

activity of Fe₃O₄/NiO-C, characterized by its extremely low overpotential 240 mV and 280 mV at the current density of 100 mA/cm² and 500 mA/cm² with swift reaction kinetics (Tafel slope of 59 mV/dec at 100 mA/cm² and 49 mV/dec at 500 mA/cm²). Furthermore, the electrocatalytic activity of Fe₃O₄/NiO-C is far better than IrO₂ as well as that of other reported literature on MOF and transition metal oxides.⁹²⁻⁹⁴ Fig 27(c) shows a comparison of overpotential at different current densities. The overpotential of the pure MOF was higher than at Fe₃O₄/NiO/Ni-Fe-MOF and Fe₃O₄/NiO-C at 100 and 500 mA cm⁻². Furthermore, the current density of 600 mA cm⁻² was achieved in the case of Fe₃O₄/NiO-C at 280 mV indicating its superior catalytic activity as compared to all the samples Ni-Fe-MOF, Fe₃O₄/NiO/Ni-Fe-MOF and IrO₂. The electrocatalytic stability of these catalysts was evaluated for 13 hrs.; the results are presented in Fig 27(d). The chronoamperometry of these samples indicates high retention rate of 82%, 84.2% and 87% for Ni-Fe-MOF, Fe₃O₄/NiO/Ni-Fe-MOF and Fe₃O₄/NiO-C, respectively. Additionally, a chronoamperometry test of Fe₃O₄/NiO-C for 24 hrs. was conducted and the incited graph in Fig 27(d) shows the retention rate of Fe₃O₄/NiO-C for 24 hrs. at 0.7V is 86%. The conductivity of these samples was evaluated using electrochemical impedance spectroscopy, Nyquist plot of Ni-Fe-MOF, Fe₃O₄/NiO/Ni-Fe-MOF and Fe₃O₄/NiO-C are presented in Fig. 27(e).

All the samples showed single semicircles starting from origin indicating negligible solution resistance. The diameter of these circular arcs was found in the following order: Ni-Fe-MOF > Fe₃O₄/NiO /Ni-Fe-MOF > Fe₃O₄/NiO -C. The intersection of the semicircular arc at the lower frequency end indicates the charge transfer resistance of an electrode material. The charge transfer resistance (R_{ct}) for Ni-Fe-MOF, Fe₃O₄/NiO /Ni-Fe-MOF and Fe₃O₄/NiO-C was found to be 2.142 Ω, 1.15 Ω and 0.595 Ω, respectively. The lowest R_{ct} value for Fe₃O₄/NiO-C, implies that Fe₃O₄/NiO-C based electrode efficiently facilitates the electron transfer as compared to other electrode materials. Furthermore, the smallest semicircle of this electrode material reveals lower impedance of Fe₃O₄/NiO-C. Comparison of overpotentials MOF-derived Fe₃O₄/NiO nanocomposites versus other iron and nickel oxide-based material is shown in Fig. 27 (f).

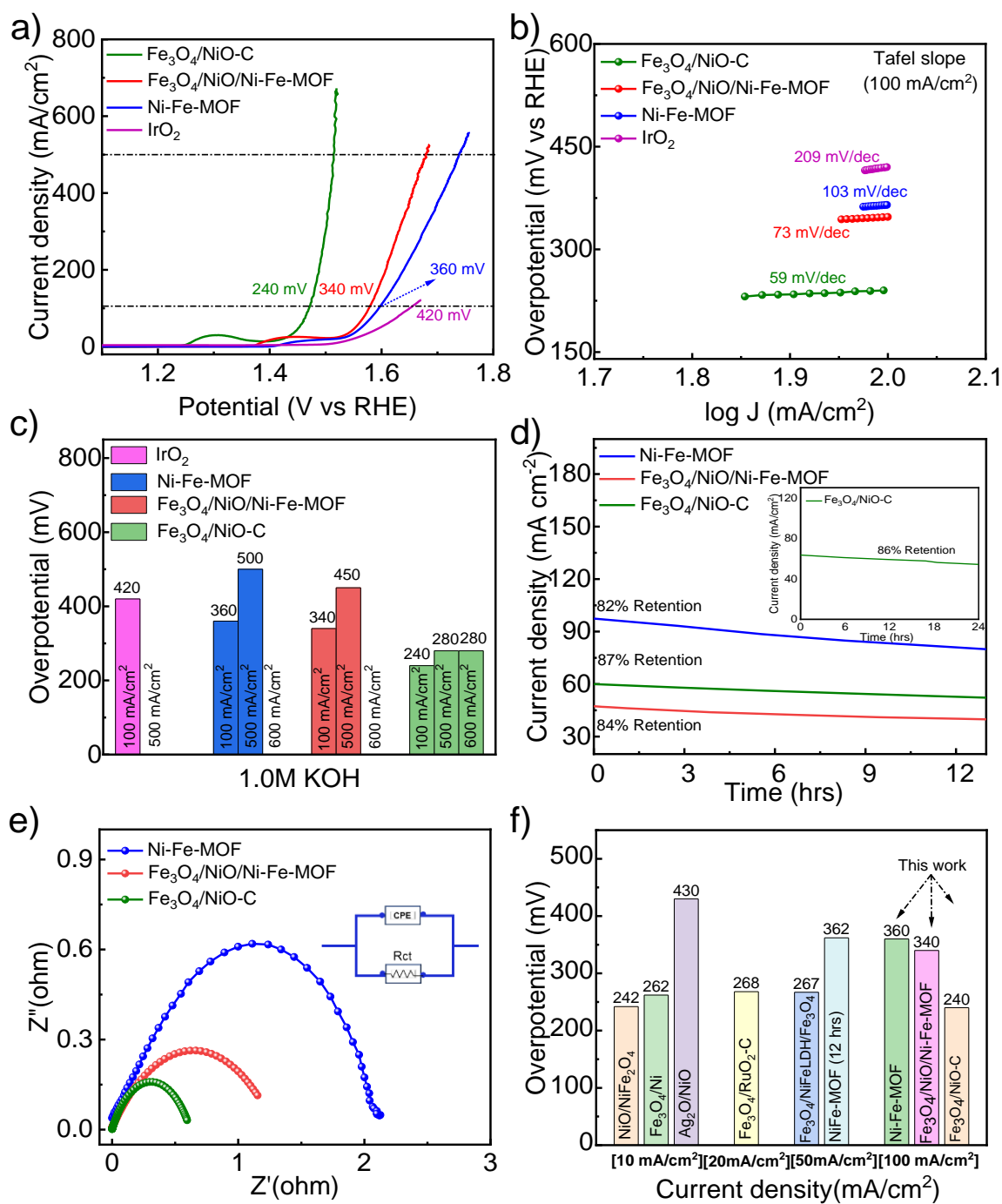


Figure 27: (a-d) Electrochemical measurements showing comprehensive analysis towards OER for Ni-Fe-MOF, Fe₃O₄/NiO/Ni-Fe-MOF and Fe₃O₄/NiO-C. (a) over potential of Ni-Fe-MOF, Fe₃O₄/NiO/Ni-Fe-MOF and Fe₃O₄/NiO-C, (b) Tafel slope of Ni-Fe-MOF, Fe₃O₄/NiO/Ni-Fe-MOF and Fe₃O₄/NiO-C, (c) comparison of overpotential at different current densities of all the samples, (d) chronoamperometry of Ni-Fe-MOF, Fe₃O₄/NiO/Ni-Fe-MOF and Fe₃O₄/NiO-C. Fig. (a-e) unveils the potential of Fe₃O₄/NiO-C for OER as an electrocatalyst keeping in view its overpotential, Tafel slope, stability and conductivity. Fig. (f) shows the OER overpotential comparison of MOF-derived Fe₃O₄/NiO nanocomposites with other iron and nickel oxide-based electrocatalysts.^{69,71,72,74-76}

HER performance of all the samples at a scan rate of 10 mV/s was also tested and the results are shown in Fig. 28(a-f). The overpotential and Tafel slope of Ni-Fe MOF, Fe₃O₄/NiO/Ni-Fe-MOF and Fe₃O₄/NiO-C are presented in Fig. 28(a) and 28(b). Along with our prepared electrocatalyst HER performance of platinum wire is also tested for comparison and presented in Fig 28(a). Ni-Fe-MOF showed an overpotential of 268 mV with a Tafel slope of 54.5 mV/dec at 10 mA/cm² indicating its potential for HER. The slight oxidation of MOF into Fe₃O₄/NiO/Ni-Fe-MOF improved the overpotential to 210 mV, however, relatively higher Tafel slope and larger semicircle in EIS of the oxides-MOF composite showed its sluggish reaction kinetics. These findings suggest that Fe₃O₄/NiO/Ni-Fe-MOF is not as promising for HER applications as it is for OER. Fe₃O₄/NiO-C showed an extremely low overpotential of 147 mV with an improved Tafel slope of 53 mV/dec at 10 mA/cm² along with the lower impedance of Fe₃O₄/NiO-C at -0.15V (shown in Fig. 28(e)) indicating it to be an energy-efficient electrocatalyst for HER. This type of catalyst is advantageous because it combines excellent performance with reasonable reaction kinetics. The comparison of the overpotential value at the current density of 10 mA/cm² with platinum wire is presented in Fig. 28(c), illustrating the superior catalytic activity of MOF derived Fe₃O₄/NiO-C. These results underscore the exceptional potential of Fe₃O₄/NiO-C as bifunctional electrocatalyst for water splitting application. Fe₃O₄/NiO-C exhibited the highest catalytic activity for OER and HER performance, as demonstrated by its lowest overpotential, impedance and Tafel slope value. Furthermore, the electrochemical stability of Fe₃O₄/NiO-C was found to be superior as compared to its precursor MOF even after 24 hours of chronoamperometry test the retention rate is 93% which is excellent (Fig. 28d & 28f).

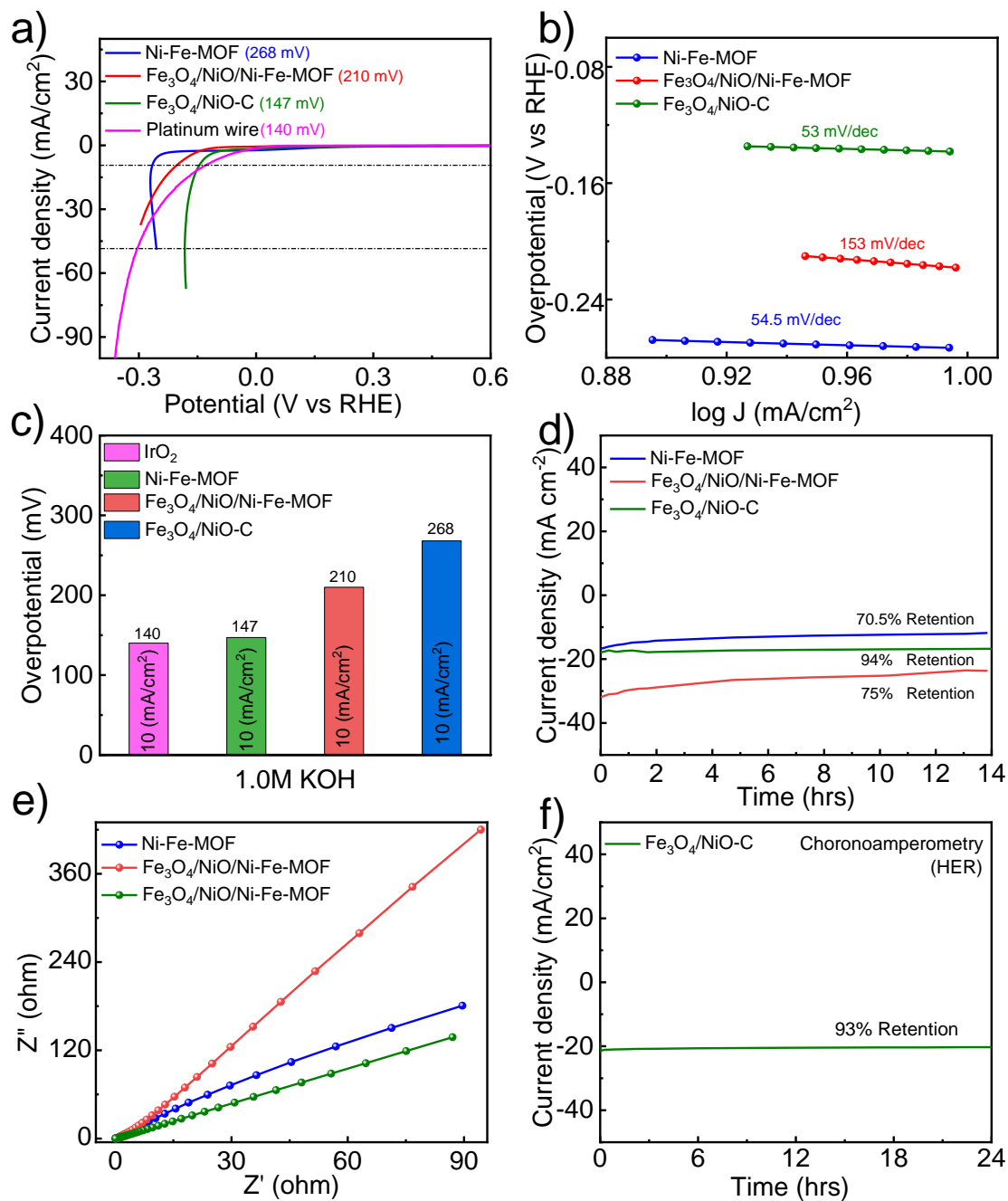


Figure 28: (a-f) Electrochemical measurement of Ni-Fe-MOF, Fe₃O₄/NiO/Ni-Fe-MOF and Fe₃O₄/NiO-C as HER catalyst. The potential of Fe₃O₄/NiO-C compared to pristine Ni-Fe-MOF for HER is demonstrated by its lowest overpotential (a-c), Tafel slope (b), high stability (d,f) and faster reaction kinetics indicated by smallest semicircle in EIS conducted at -0.15 V (e)

The removal of the organic ligand during the transformation from MOF to oxides results in nanosized particles with exposed metal sites and, highly conductive structure because of the graphitized carbon. Furthermore, the controllable synthesis of MOFs allows for the optimization of the precursor compositions, which can open new avenues for designing and optimizing the properties of oxides based on electrocatalysts with superior performance. Table 1 presents a comparison of the HER and OER activities of our electrocatalysts (Fe-Ni-MOF, Fe₃O₄/NiO/Ni-Fe-MOF, and Fe₃O₄/NiO-C) with those of other recently reported Fe and Ni-based catalysts in a

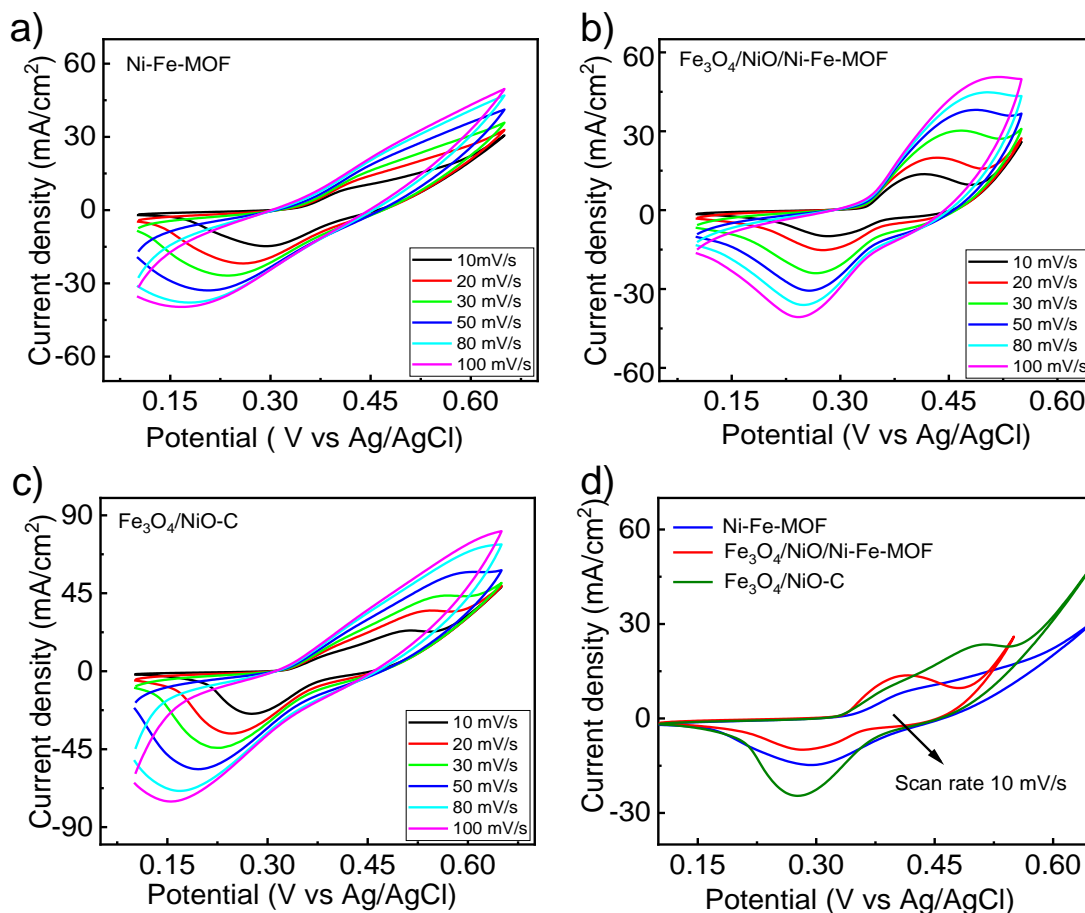


Figure 29: Cyclic voltammetry curves showcasing the redox peaks of Ni-Fe-MOF, Fe₃O₄/NiO/Ni-Fe-MOF and Fe₃O₄/NiO-C electrocatalyst.

1M KOH electrolyte.

Cyclic voltammetry (CV) was also performed at different scan rates ranging from 10 mV/s to 100 mV/s to evaluate the redox properties Fe-Ni-MOF, Fe₃O₄/NiO/Ni-Fe-MOF, and Fe₃O₄/NiO-C and the results are shown in Fig. 29(a-d). The potential window was 0.1 to 0.65 V for Fe-Ni-MOF and Fe₃O₄/NiO-C, and 0.1 to 0.55 V for Fe₃O₄/NiO/Ni-Fe-MOF shown in Fig. 29(a-c). Obvious redox reactions with OH⁻ between Ni²⁺ and Ni³⁺ can be seen in Fig. 29(d) where all the electrodes exhibit a pair of strong redox peaks with different current densities at a scan rate of 10 mV/s. The oxidative peak position in Fe₃O₄/NiO-C was observed at a higher potential than Fe-Ni-MOF and Fe₃O₄/NiO/Ni-Fe-MOF as the energy required to oxidize Ni²⁺ to a higher oxidation state in the oxide form (NiO) is typically higher than that in Ni-MOF due to the stabilization of the Ni²⁺ state by the oxide lattice⁹⁵. Moreover, Fe₃O₄/NiO-C shows a much higher current density than Fe-Ni-MOF and Fe₃O₄/NiO/Ni-Fe-MOF, indicating the exceptional pseudocapacitive behavior of Fe₃O₄/NiO-C.⁹⁶

Conclusion

In this work we synthesized $\text{Fe}_3\text{O}_4/\text{NiO}/\text{Ni-Fe-MOF}$ and $\text{Fe}_3\text{O}_4/\text{NiO-C}$ using the pyrolysis of Ni-Fe-MOF. XRD analysis confirms the synthesis of MOF and its conversion into $\text{Fe}_3\text{O}_4/\text{NiO}/\text{Ni-Fe-MOF}$ and $\text{Fe}_3\text{O}_4/\text{NiO-C}$. The morphological analysis revealed the flower-like structure of pure MOF and porous nature of derived nanocomposites. The conversion of Ni-Fe-MOF into Fe_3O_4 and NiO nanocomposite resulted in higher specific surface area. The electrocatalytic performance of $\text{Fe}_3\text{O}_4/\text{NiO-C}$ was found superior as compared to its MOF precursor. These results disclose the potential of $\text{Fe}_3\text{O}_4/\text{NiO-C}$ as an outstanding bifunctional electrocatalyst, surpassing commercial catalysts. In case of OER it achieves an ultra-high current density of 600 mA/cm^2 at 280 mV overpotential and an overpotential of 147 mV at a current density of 10 mA/cm^2 for HER. Furthermore, it maintains high stability in both OER and HER. The exceptional activity of $\text{Fe}_3\text{O}_4/\text{NiO-C}$ catalyst is attributed to the synergistic interplay of its oxide components improved conductivity due to graphitized carbon, porous structure, and high electrochemical surface area. This study provides valuable insights for designing oxides-based highly active electrocatalysts, which offer a controllable synthesis of precursors because of the customizable nature of MOFs.

Chapter 6

Future Recommendation & Publication

1. Future Recommendation

- a) CV and GCD testing can be performed to check the capacitance and efficiency of Fe₃O₄/NiO-C as a pseudo supercapacitor.
- b) It is worthwhile to investigate the synergistic integration of other MOF-derived transition metal oxides as it can unveil novel opportunities for water electrolysis and energy storage as a result of this transformative process.

2. Published Articles

- a) Iqbal, Z., Sonadia, Miran, W., Ul-Hamid, A., Sohail, M., & Azad, F. (2024). Tailored Flower-Like Ni-Fe-MOF-Derived oxide Composites: Highly active and durable electrocatalysts for overall water splitting. *Fuel*, 372.
<https://doi.org/10.1016/j.fuel.2024.132112>
- b) Sonadia, Iqbal, Z., Miran, W., Ul-Hamid, A., Ayub, K. S., & Azad, F. (2024). Enhanced Electrocatalytic Performance of Erbium-Incorporated Nickel-Based Metal–Organic Frameworks for Water Splitting. *Energy & Fuels*, 38(6), 5397–5406.

3. Articles writing process

- a) GQDs coated MOF derived oxides composite as supercapacitor electrode material for electrochemical energy storage and oxygen evolution reaction.
- b) A novel Carbon nanotube coupled Zn bimetallic MOF composite: highly active electrocatalyst with ultra-high current density for Oxygen Evolution Reaction.

References

1. Hohlwegler, P. Bioeconomy and Food Security: Moral Conflicts Caused by Climate Change and Population Growth. in *Bioeconomy and Sustainability: Perspectives from Natural and Social Sciences, Economics and Ethics* 61–75 (Springer, 2022).
2. Moriarty, P. & Honnery, D. Future Energy. in *Switching Off: Meeting Our Energy Needs in A Constrained Future* 55–71 (Springer, 2022).
3. Naheed, S. An overview of the influence of climate change on food security and human health. *life* **3**, 15 (2023).
4. Shi, Y. & Zhang, B. Recent advances in transition metal phosphide nanomaterials: synthesis and applications in hydrogen evolution reaction. *Chem Soc Rev* **45**, 1529–1541 (2016).
5. Wang, W., Xu, X., Zhou, W. & Shao, Z. Recent progress in metal-organic frameworks for applications in electrocatalytic and photocatalytic water splitting. *Advanced science* **4**, 1600371 (2017).
6. Dincer, I. & Acar, C. A review on clean energy solutions for better sustainability. *Int J Energy Res* **39**, 585–606 (2015).
7. Wakeel, M., Chen, B. & Jahangir, S. Overview of energy portfolio in Pakistan. *Energy Procedia* **88**, 71–75 (2016).
8. Adams, S., Klobodu, E. K. M. & Apio, A. Renewable and non-renewable energy, regime type and economic growth. *Renew Energy* **125**, 755–767 (2018).
9. Dai, S. *et al.* Optimization of Pt–Oxygen-Containing Species Anodes for Ethanol Oxidation Reaction: High Performance of Pt-AuSnO_x Electrocatalyst. *J Phys Chem Lett* **11**, 2846–2853 (2020).
10. Acar, C. & Dincer, I. Review and evaluation of hydrogen production options for better environment. *J Clean Prod* **218**, 835–849 (2019).
11. Abdalla, A. M. *et al.* Hydrogen production, storage, transportation and key challenges with applications: A review. *Energy Convers Manag* **165**, 602–627 (2018).
12. Johnston, B., Mayo, M. C. & Khare, A. Hydrogen: the energy source for the 21st century. *Technovation* **25**, 569–585 (2005).
13. Arregi, A., Amutio, M., Lopez, G., Bilbao, J. & Olazar, M. Evaluation of thermochemical routes for hydrogen production from biomass: A review. *Energy Convers Manag* **165**, 696–719 (2018).

14. Kothari, R., Buddhi, D. & Sawhney, R. L. Comparison of environmental and economic aspects of various hydrogen production methods. *Renewable and Sustainable Energy Reviews* **12**, 553–563 (2008).
15. Acar, C. & Dincer, I. Comparative assessment of hydrogen production methods from renewable and non-renewable sources. *Int J Hydrogen Energy* **39**, 1–12 (2014).
16. Roeb, M. *et al.* Materials-related aspects of thermochemical water and carbon dioxide splitting: a review. *Materials* **5**, 2015–2054 (2012).
17. Rosen, M. A. Advances in hydrogen production by thermochemical water decomposition: a review. *Energy* **35**, 1068–1076 (2010).
18. Anantharaj, S. *et al.* Recent trends and perspectives in electrochemical water splitting with an emphasis on sulfide, selenide, and phosphide catalysts of Fe, Co, and Ni: a review. *ACS Catal* **6**, 8069–8097 (2016).
19. Yan, Y., Xia, B. Y., Zhao, B. & Wang, X. A review on noble-metal-free bifunctional heterogeneous catalysts for overall electrochemical water splitting. *J Mater Chem A Mater* **4**, 17587–17603 (2016).
20. Fei, J. & Li, J. Controlled preparation of porous TiO₂-Ag nanostructures through supramolecular assembly for plasmon-enhanced photocatalysis. *Adv Mater* **27**, 314–319 (2014).
21. Lu, B., Li, X., Wang, T., Xie, E. & Xu, Z. WO₃ nanoparticles decorated on both sidewalls of highly porous TiO₂ nanotubes to improve UV and visible-light photocatalysis. *J Mater Chem A Mater* **1**, 3900–3906 (2013).
22. Wang, S. & Wang, X. Multifunctional metal–organic frameworks for photocatalysis. *small* **11**, 3097–3112 (2015).
23. Liang, Q. *et al.* Macroscopic 3D porous graphitic carbon nitride monolith for enhanced photocatalytic hydrogen evolution. *Adv Mater* **27**, 4634–4639 (2015).
24. Yu, J. G., Su, Y. R. & Cheng, B. Template-free fabrication and enhanced photocatalytic activity of hierarchical macro-/mesoporous titania. *Adv Funct Mater* **17**, 1984–1990 (2007).
25. Chen, C. *et al.* Synthesis of visible-light responsive graphene oxide/TiO₂ composites with p/n heterojunction. *ACS Nano* **4**, 6425–6432 (2010).
26. Cho, Y. *et al.* Multiple heterojunction in single titanium dioxide nanoparticles for novel metal-free photocatalysis. *Nano Lett* **18**, 4257–4262 (2018).
27. Zhang, Z. *et al.* Electrospun nanofibers of p-type NiO/n-type ZnO heterojunctions with enhanced photocatalytic activity. *ACS Appl Mater Interfaces* **2**, 2915–2923 (2010).

28. Rehman, A., Farrukh, S., Hussain, A. & Pervaiz, E. Synthesis and effect of metal–organic frameworks on CO₂ adsorption capacity at various pressures: a contemplating review. *Energy & environment* **31**, 367–388 (2020).
29. Li, H. *et al.* Recent advances in gas storage and separation using metal–organic frameworks. *Materials Today* **21**, 108–121 (2018).
30. Zhang, Y. *et al.* Luminescent sensors based on metal-organic frameworks. *Coord Chem Rev* **354**, 28–45 (2018).
31. Khan, N. A., Hasan, Z. & Jhung, S. H. Adsorptive removal of hazardous materials using metal-organic frameworks (MOFs): a review. *J Hazard Mater* **244**, 444–456 (2013).
32. Jiao, L., Wang, Y., Jiang, H. & Xu, Q. Metal–organic frameworks as platforms for catalytic applications. *Advanced Materials* **30**, 1703663 (2018).
33. Fang, Y. *et al.* Metal–organic frameworks for solar energy conversion by photoredox catalysis. *Coord Chem Rev* **373**, 83–115 (2018).
34. Meyer, K., Ranocchiari, M. & van Bokhoven, J. A. Metal organic frameworks for photo-catalytic water splitting. *Energy Environ Sci* **8**, 1923–1937 (2015).
35. Fujishima, A. & Honda, K. TiO₂ photoelectrochemistry and photocatalysis. *Nature* **238**, 37–38 (1972).
36. Audichon, T. *et al.* IrO₂ coated on RuO₂ as efficient and stable electroactive nanocatalysts for electrochemical water splitting. *The Journal of Physical Chemistry C* **120**, 2562–2573 (2016).
37. Fărcaș, A. C. & Dobra, P. Adaptive Control of Membrane Conductivity of PEM Fuel Cell. *Procedia Technology* **12**, 42–49 (2014).
38. You, B. & Sun, Y. Innovative strategies for electrocatalytic water splitting. *Acc Chem Res* **51**, 1571–1580 (2018).
39. Wang, J. *et al.* Recent progress in cobalt-based heterogeneous catalysts for electrochemical water splitting. *Advanced materials* **28**, 215–230 (2016).
40. Dhakshinamoorthy, A., Li, Z. & Garcia, H. Catalysis and photocatalysis by metal organic frameworks. *Chem Soc Rev* **47**, 8134–8172 (2018).
41. Gong, M. & Dai, H. A mini review of NiFe-based materials as highly active oxygen evolution reaction electrocatalysts. *Nano Res* **8**, 23–39 (2015).
42. Lan, Z.-A., Zhang, G. & Wang, X. A facile synthesis of Br-modified g-C₃N₄ semiconductors for photoredox water splitting. *Appl Catal B* **192**, 116–125 (2016).
43. Busch, M. *et al.* Beyond the top of the volcano?—A unified approach to electrocatalytic oxygen reduction and oxygen evolution. *Nano Energy* **29**, 126–135 (2016).

44. Wang, Q. & Astruc, D. State of the art and prospects in metal–organic framework (MOF)-based and MOF-derived nanocatalysis. *Chem Rev* **120**, 1438–1511 (2019).
45. Furukawa, H. *et al.* Ultrahigh porosity in metal-organic frameworks. *Science (1979)* **329**, 424–428 (2010).
46. Silva, P., Vilela, S. M. F., Tomé, J. P. C. & Paz, F. A. A. Multifunctional metal–organic frameworks: from academia to industrial applications. *Chem Soc Rev* **44**, 6774–6803 (2015).
47. Wang, Z. & Cohen, S. M. Postsynthetic modification of metal–organic frameworks. *Chem Soc Rev* **38**, 1315–1329 (2009).
48. Kim, C. R., Uemura, T. & Kitagawa, S. Inorganic nanoparticles in porous coordination polymers. *Chem Soc Rev* **45**, 3828–3845 (2016).
49. Furukawa, H., Cordova, K. E., O’Keeffe, M. & Yaghi, O. M. The chemistry and applications of metal-organic frameworks. *Science (1979)* **341**, 1230444 (2013).
50. Pendashteh, A. *et al.* Bimetal zeolitic imidazolate framework (ZIF-9) derived nitrogen-doped porous carbon as efficient oxygen electrocatalysts for rechargeable Zn-air batteries. *J Power Sources* **427**, 299–308 (2019).
51. Ning, H. *et al.* Porous N-doped carbon-encapsulated CoNi alloy nanoparticles derived from MOFs as efficient bifunctional oxygen electrocatalysts. *ACS Appl Mater Interfaces* **11**, 1957–1968 (2018).
52. Wang, Z. *et al.* Core-shell carbon materials derived from metal-organic frameworks as an efficient oxygen bifunctional electrocatalyst. *Nano Energy* **30**, 368–378 (2016).
53. Li, Y. *et al.* Bimetallic zeolitic imidazolate framework derived carbon nanotubes embedded with Co nanoparticles for efficient bifunctional oxygen electrocatalyst. *Adv Energy Mater* **8**, 1702048 (2018).
54. Li, J., Kang, Y., Liu, D., Lei, Z. & Liu, P. Nitrogen-doped graphitic carbon-supported ultrafine Co nanoparticles as an efficient multifunctional electrocatalyst for HER and rechargeable Zn–air batteries. *ACS Appl Mater Interfaces* **12**, 5717–5729 (2020).
55. Wu, Y. *et al.* A metal-organic framework-derived bifunctional catalyst for hybrid sodium-air batteries. *Appl Catal B* **241**, 407–414 (2019).
56. Ding, D. *et al.* Multi-level architecture optimization of MOF-templated Co-based nanoparticles embedded in hollow N-doped carbon polyhedra for efficient OER and ORR. *ACS Catal* **8**, 7879–7888 (2018).
57. Li, X. *et al.* ZIF-67-derived Co₃O₄@ carbon protected by oxygen-buffering CeO₂ as an efficient catalyst for boosting oxygen reduction/evolution reactions. *J Mater Chem A Mater* **7**, 25853–25864 (2019).

58. Yang, L., Wang, D., Lv, Y. & Cao, D. Nitrogen-doped graphitic carbons with encapsulated CoNi bimetallic nanoparticles as bifunctional electrocatalysts for rechargeable Zn–Air batteries. *Carbon NY* **144**, 8–14 (2019).
59. Wan, J. *et al.* Facile synthesis of CoNi_x nanoparticles embedded in nitrogen–carbon frameworks for highly efficient electrocatalytic oxygen evolution. *Chemical Communications* **53**, 12177–12180 (2017).
60. Fu, X. *et al.* Tailoring FeN₄ sites with edge enrichment for boosted oxygen reduction performance in proton exchange membrane fuel cell. *Adv Energy Mater* **9**, 1803737 (2019).
61. Khani, H., Grundish, N. S., Wipf, D. O. & Goodenough, J. B. Graphitic-shell encapsulation of metal electrocatalysts for oxygen evolution, oxygen reduction, and hydrogen evolution in alkaline solution. *Adv Energy Mater* **10**, 1903215 (2020).
62. Peng, H. *et al.* Effect of transition metals on the structure and performance of the doped carbon catalysts derived from polyaniline and melamine for ORR application. *ACS Catal* **4**, 3797–3805 (2014).
63. Zhang, L., Xiao, J., Wang, H. & Shao, M. Carbon-based electrocatalysts for hydrogen and oxygen evolution reactions. *ACS Catal* **7**, 7855–7865 (2017).
64. Zou, H., Li, G., Duan, L., Kou, Z. & Wang, J. In situ coupled amorphous cobalt nitride with nitrogen-doped graphene aerogel as a trifunctional electrocatalyst towards Zn-air battery driven full water splitting. *Appl Catal B* **259**, 118100 (2019).
65. Ye, W. *et al.* 2D cocrystallized metal–organic nanosheet array as an efficient and stable bifunctional electrocatalyst for overall water splitting. *ACS Sustain Chem Eng* **7**, 18085–18092 (2019).
66. Fu, G. *et al.* Boosting bifunctional oxygen electrocatalysis with 3D graphene aerogel-supported Ni/MnO particles. *Advanced Materials* **30**, 1704609 (2018).
67. Yu, Y. *et al.* Reconciling of experimental and theoretical insights on the electroactive behavior of C/Ni nanoparticles with AuPt alloys for hydrogen evolution efficiency and Non-enzymatic sensor. *Chemical Engineering Journal* **435**, (2022).
68. Oh, Y. *et al.* Pulsed laser interference patterning of transition-metal carbides for stable alkaline water electrolysis kinetics. *Carbon Energy* (2024) doi:10.1002/cey2.448.
69. Shaghghi, Z. & Akbari, S. Hydrogen and oxygen production on Ag₂O/NiO hybrid nanostructures via electrochemical water splitting. *Int J Hydrogen Energy* **51**, 936–949 (2024).
70. Naik Shreyanka, S., Theerthagiri, J., Lee, S. J., Yu, Y. & Choi, M. Y. Multiscale design of 3D metal–organic frameworks (M–BTC, M: Cu, Co, Ni) via PLAL enabling bifunctional electrocatalysts for robust overall water splitting. *Chemical Engineering Journal* **446**, (2022).

71. Weng, S., An, Q., Xu, Y., Jiao, Y. & Chen, J. In-Situ Formation of NiFe-MOF on Nickel Foam as a Self-Supporting Electrode for Flexible Electrochemical Sensing and Energy Conversion. *Chemosensors* **11**, (2023).
72. Zhang, X. *et al.* Sandwich structured Fe₃O₄/NiFe LDH/Fe₃O₄ as a bifunctional electrocatalyst with superior stability for highly sustained overall water splitting. *J Alloys Compd* **932**, 167612 (2023).
73. Indra, A., Menezes, P. W., Zaharieva, I., Dau, H. & Driess, M. Detecting structural transformation of cobalt phosphonate to active bifunctional catalysts for electrochemical water-splitting. *J Mater Chem A Mater* **8**, 2637–2643 (2020).
74. Shekhawat, A., Samanta, R. & Barman, S. MOF-Derived Porous Fe₃O₄/RuO₂-C Composite for Efficient Alkaline Overall Water Splitting. *ACS Appl Energy Mater* (2022) doi:10.1021/acsaem.2c00471.
75. Jesudass, S. C. *et al.* Bimetallic NiO/NiFe₂O₄ heterostructures with interfacial effects for boosting electrochemical water splitting applications. *Journal of Electroanalytical Chemistry* **952**, 117947 (2024).
76. Zhu, F., Wang, Y., Chen, Y., Wu, M. & Jiang, W. Magnetic Field-Assisted Electrodeposition of Fe₃O₄ Nanoparticles on Ni as Bifunctional Electrocatalyst for Overall Water Splitting. *ACS Appl Nano Mater* **6**, 19837–19847 (2023).
77. Baig, N., Kammakakam, I., Falath, W. & Kammakakam, I. Nanomaterials: A review of synthesis methods, properties, recent progress, and challenges. *Materials Advances* vol. 2 1821–1871 Preprint at <https://doi.org/10.1039/d0ma00807a> (2021).
78. Anantha Padmanaban, D. Summary of Some Selected Characterization Methods of Geopolymers. in (2018). doi:10.5772/intechopen.82208.
79. Luo, Y. *et al.* Structural and Electronic Modulation of Iron-Based Bimetallic Metal-Organic Framework Bifunctional Electrocatalysts for Efficient Overall Water Splitting in Alkaline and Seawater Environment. *ACS Appl Mater Interfaces* **14**, 46374–46385 (2022).
80. Vu, T. A. *et al.* Highly photocatalytic activity of novel Fe-MIL-88B/GO nanocomposite in the degradation of reactive dye from aqueous solution. *Mater Res Express* **4**, (2017).
81. Li, X., Guo, W., Liu, Z., Wang, R. & Liu, H. Fe-based MOFs for efficient adsorption and degradation of acid orange 7 in aqueous solution via persulfate activation. *Appl Surf Sci* **369**, 130–136 (2016).
82. Zheng, F. *et al.* Fe/Ni bimetal organic framework as efficient oxygen evolution catalyst with low overpotential. *J Colloid Interface Sci* **555**, 541–547 (2019).

83. Shekhawat, A., Samanta, R. & Barman, S. MOF-Derived Porous Fe₃O₄/RuO₂-C Composite for Efficient Alkaline Overall Water Splitting. *ACS Appl Energy Mater* (2022) doi:10.1021/acsaem.2c00471.
84. Wardani, M., Yulizar, Y., Abdullah, I. & Bagus Apriandanu, D. O. Synthesis of NiO nanoparticles via green route using *Ageratum conyzoides* L. leaf extract and their catalytic activity. in *IOP Conference Series: Materials Science and Engineering* vol. 509 (Institute of Physics Publishing, 2019).
85. Zhuang, L. *et al.* Preparation and characterization of Fe₃O₄ particles with novel nanosheets morphology and magnetochromatic property by a modified solvothermal method. *Sci Rep* **5**, (2015).
86. Abd, A., S.Ali, R. & Hussein, A. Fabrication And Characterization Of Nickel Oxide Nanoparticles/Silicon Heterojunction. *Journal of Multidisciplinary Engineering Science Studies (JMESS)* **2**, 434–440 (2016).
87. Zhang, Y. *et al.* Room-Temperature Mixed-Potential Type ppb-Level NO Sensors Based on K₂Fe₄O₇ Electrolyte and Ni/Fe–MOF Sensing Electrodes. *ACS Sens* **6**, 4435–4442 (2021).
88. Le, V. T., Tran, V. A., Tran, D. L., Nguyen, T. L. H. & Doan, V. D. Fabrication of Fe₃O₄/CuO@C composite from MOF-based materials as an efficient and magnetically separable photocatalyst for degradation of ciprofloxacin antibiotic. *Chemosphere* **270**, (2021).
89. KURNAZ YETİM, N. Catalytic Properties of Hydrothermally Synthesized Flower-like NiO@Fe₃O₄. *Düzce Üniversitesi Bilim ve Teknoloji Dergisi* **8**, 1964–1974 (2020).
90. Rashid, S. *et al.* Graphene quantum dots (GQDs) decorated Co-Zn ferrite: Structural, morphological, dielectric, and magnetic properties. *J Magn Magn Mater* **570**, (2023).
91. Ogundipe, T. O. *et al.* Nickel-cobalt phosphide terephthalic acid nano-heterojunction as excellent bifunctional electrocatalyst for overall water splitting. *Electrochim Acta* **421**, 140484 (2022).
92. Shabbir, B. *et al.* Facile synthesis of Er-MOF/Fe₂O₃ nanocomposite for oxygen evolution reaction. *Mater Chem Phys* **292**, 126861 (2022).
93. Jiang, J. *et al.* Fe₂O₃ nanocatalysts on N-doped carbon nanomaterial for highly efficient electrochemical hydrogen evolution in alkaline. *J Power Sources* **426**, 74–83 (2019).
94. Jesudass, S. C. *et al.* Defect engineered ternary metal spinel-type Ni-Fe-Co oxide as bifunctional electrocatalyst for overall electrochemical water splitting. *J Colloid Interface Sci* (2024) doi:10.1016/j.jcis.2024.02.042.
95. Wan, J. *et al.* Transition Bimetal Based MOF Nanosheets for Robust Aqueous Zn Battery. *Front Mater* **7**, (2020).

96. Sanati, S., Rezvani, Z. & Habibi, B. The NiGa-LDH@NiWO₄ nanocomposite as an electrode material for pseudocapacitors. *New Journal of Chemistry* **42**, 18426–18436 (2018).
97. Naimi, Y. & Antar, A. Hydrogen generation by water electrolysis. *Advances in hydrogen generation technologies* **1**, (2018).
98. Ojeda, J. J. & Dittrich, M. Fourier transform infrared spectroscopy for molecular analysis of microbial cells. *Methods in Molecular Biology* **881**, 187–211 (2012).
99. Thummar, K., Abang, R., Menzel, K. & De Groot, M. T. Coupling a Chlor-Alkali Membrane Electrolyzer Cell to a Wind Energy Source: Dynamic Modeling and Simulations. *Energies (Basel)* **15**, (2022).
100. Pirozzi, N. M., Kuipers, J. & Giepmans, B. N. G. Chapter 5 - Sample preparation for energy dispersive X-ray imaging of biological tissues. in *Methods in Cell Biology* (eds. Müller-Reichert, T. & Verkade, P.) vol. 162 89–114 (Academic Press, 2021).